Electronic Supplementary information

Fluorescent molecular probe for *in vivo* targeting and live cell imaging of the intracellular bacteria in a urinary tract infection model

Shailendra Koirala[a], Miguel A. Gaspar[a], Yalini H. Wijesundara[a], Dong-Hao Li[d], Jashkaran G. Gadhvi[c], Ryanne N. Ehrman[a], Samuel A. Cornelius[c], Charles Mariasoosai[a], Thien-Quang N. Nguyen[a], Orikeda Trashi[a], Ikeda Trashi[a], Sneha Kumari[a], Laurel M. Hagge[a], Thomas S. Howlett[a], Hedieh Torabifard[a], Bradley D. Smith[d], Nicole J. De Nisco[c*], and Jeremiah J. Gassensmith[a,b*]

[a] Department of Chemistry and Biochemistry, [b] Department of Biomedical Engineering, and [c] Department of Biological Sciences The University of Texas at Dallas 800 West Campbell Road, Richardson, Texas 75080-3021, United States [d] Department of Chemistry and Biochemistry University of Notre Dame 236 Nieuwland Science Hall, Notre Dame, Indiana 46556, United States Email: nicole.denisco@utdallas.edu and gassensmith@utdallas.edu

Table of Contents

Choice of Zn-Oxy-DPA rather than ZnDPA as bacteria targeting unit in BactVue

The chemical structure of **BactVue** is a charge-balanced Cy7 dye attached to **Zn-Oxy-DPA** as the bacteria targeting unit. The crucial choice of **Zn-Oxy-DPA** as the targeting unit and not **ZnDPA** was made for the following reasons.

There is almost 20 years of published literature comparing the oxyanion recognition and membrane targeting capabilities of fluorescent molecular probes with **ZnDPA** or **Zn-Oxy-DPA** as the targeting unit.[1, 2] Multiple independent studies have measured oxyanion association, partitioning between 1-octanol and water, partitioning into liposome membranes, and cell membrane permeation.[2-6] In an aqueous solution, both targeting units associate reversibly with oxyanions in the binding order of phosphate > carboxylate > nitrate. Depending on the structure of the appended fluorescent dye, both types of targeting units have weak/moderate affinity for a bilayer membrane composed entirely of zwitterionic phospholipids, and stronger membrane affinity is obtained if the membrane contains anionic polar lipids, such as fatty acids or lipid phosphates.

Independent studies have shown that a **ZnDPA** targeting unit adheres to the exterior surface of a liposome or cell membrane and does not partition into the membrane core,[2, 3] whereas a **Zn-Oxy-DPA** targeting unit readily permeates through a bilayer membrane under the same conditions, especially if the membrane contains anionic polar lipids.[3, 7] Moreover, 1-octanol/water partition experiments have shown that a **Zn-Oxy-DPA** targeting unit can associate with an anionic polar lipid to form a lipophilic ion-pair complex that partitions in the 1-octanol phase, but a **ZnDPA** targeting unit does not partition into the 1-octanol phase under the same conditions.[7-9] Not only can a lipophilic **Zn-Oxy-DPA** ion-pair complex partition into the core of a bilayer membrane, but **Zn-Oxy-DPA** ion-pair complexes with a non-cylindrical shape can disrupt bilayer membrane packing and promote membrane diffusion of other analytes in the solution.[5, 10]

The contrasting membrane permeation properties of **ZnDPA** and **Zn-Oxy-DPA** targeting units ~~is~~are readily explained by considering literature X-ray structures (Scheme S1),[11, 12] with additional insight provided by two new X-ray crystal structures reported in Scheme S2. In short, a **Zn-Oxy-DPA** targeting unit associates with oxyanions to form a compact structure that locates all the charged atoms in the core of the complex, with the two zinc cations bonded to the central phenoxy atom and simultaneously coordinated by one or two oxyanions (depend~~s~~ing on oxyanion sterics). If the coordinated oxyanions are fatty acids or lipid phosphates, then the structural periphery of

the complex is lipophilic. Thus, the complex acts like a classic membrane transport carrier and readily diffuses through a bilayer membrane (Scheme S3 *left*). In contrast, a **ZnDPA** targeting unit associates with oxyanions to form a charge-separated complex that has an extended conformation with the two zinc cations separated due to electrostatic repulsion. Even if the bound oxyanion is a polar lipid, the associated complex has an amphiphilic structure and does not partition into the hydrophobic core of a bilayer membrane (Scheme 3 *right*). Further insight is provided by the Molecular Dynamics simulations described below.

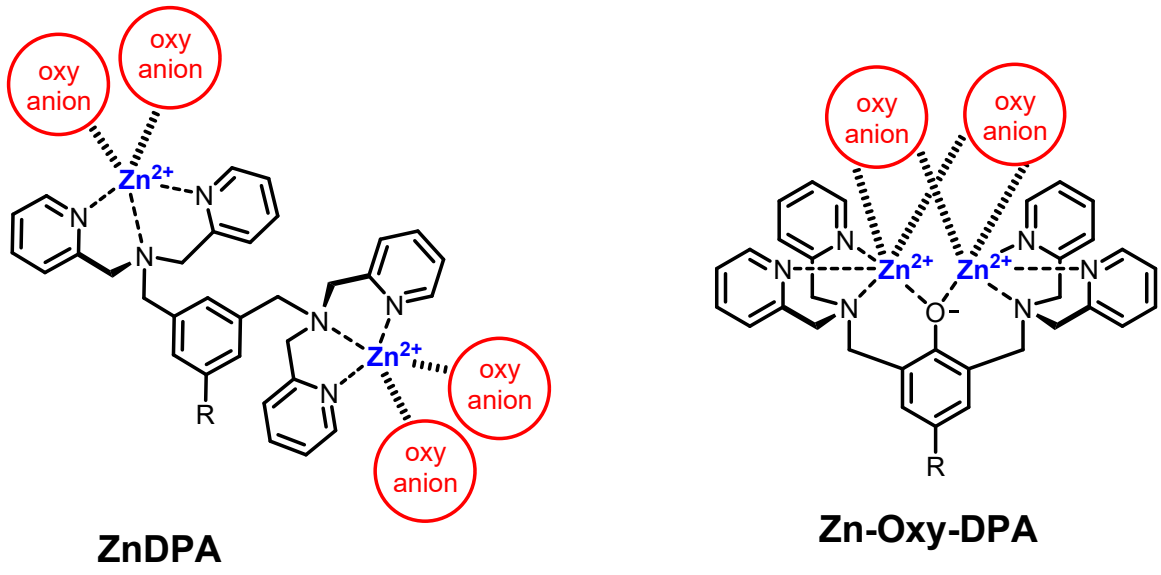

Scheme S1. Chemical pictures of literature X-ray structures showing **ZnDPA** and **Zn-Oxy-DPA** complexes with associated oxyanions.[11, 12]

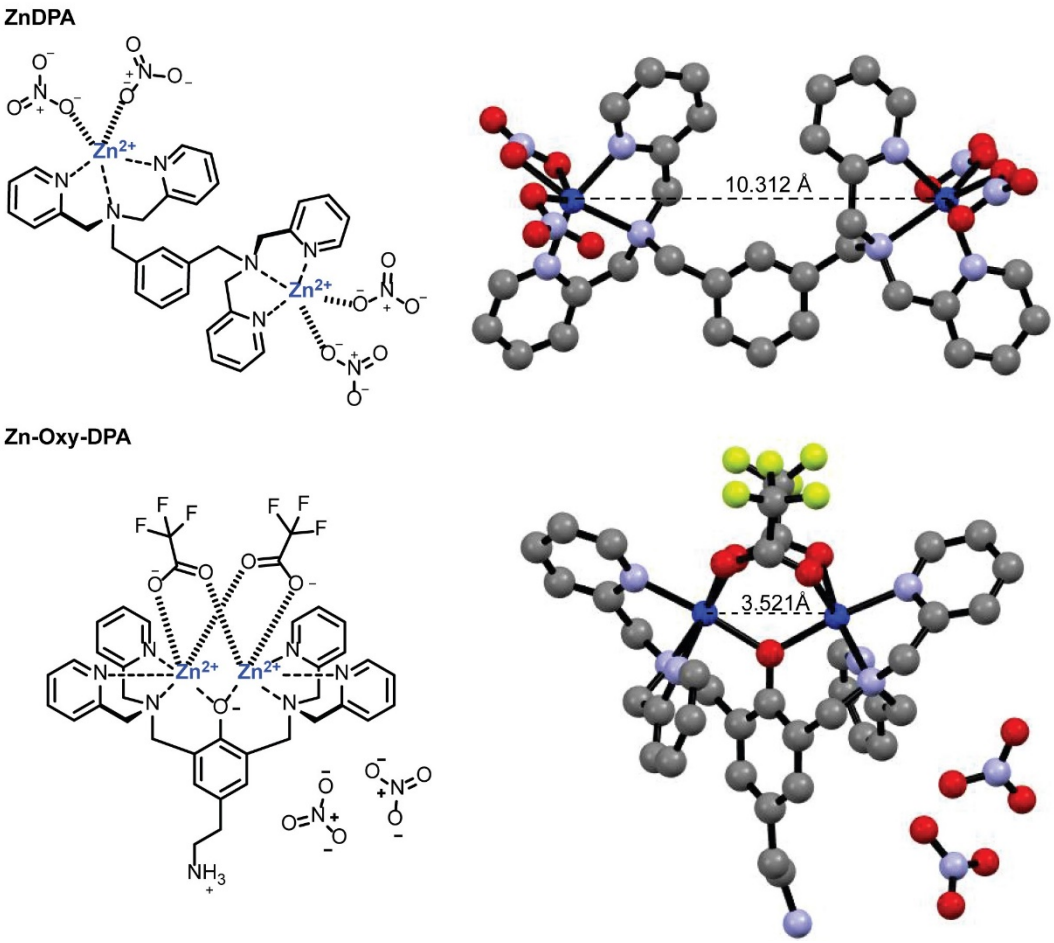

Scheme S2. X-ray crystal structures of two new model compounds. (*top*) **ZnDPA**•4NO_3 and (*bottom*) **Zn-Oxy-DPA**•2CF_3CO_2•2NO_3. These structures match the literature structures in Scheme S1.

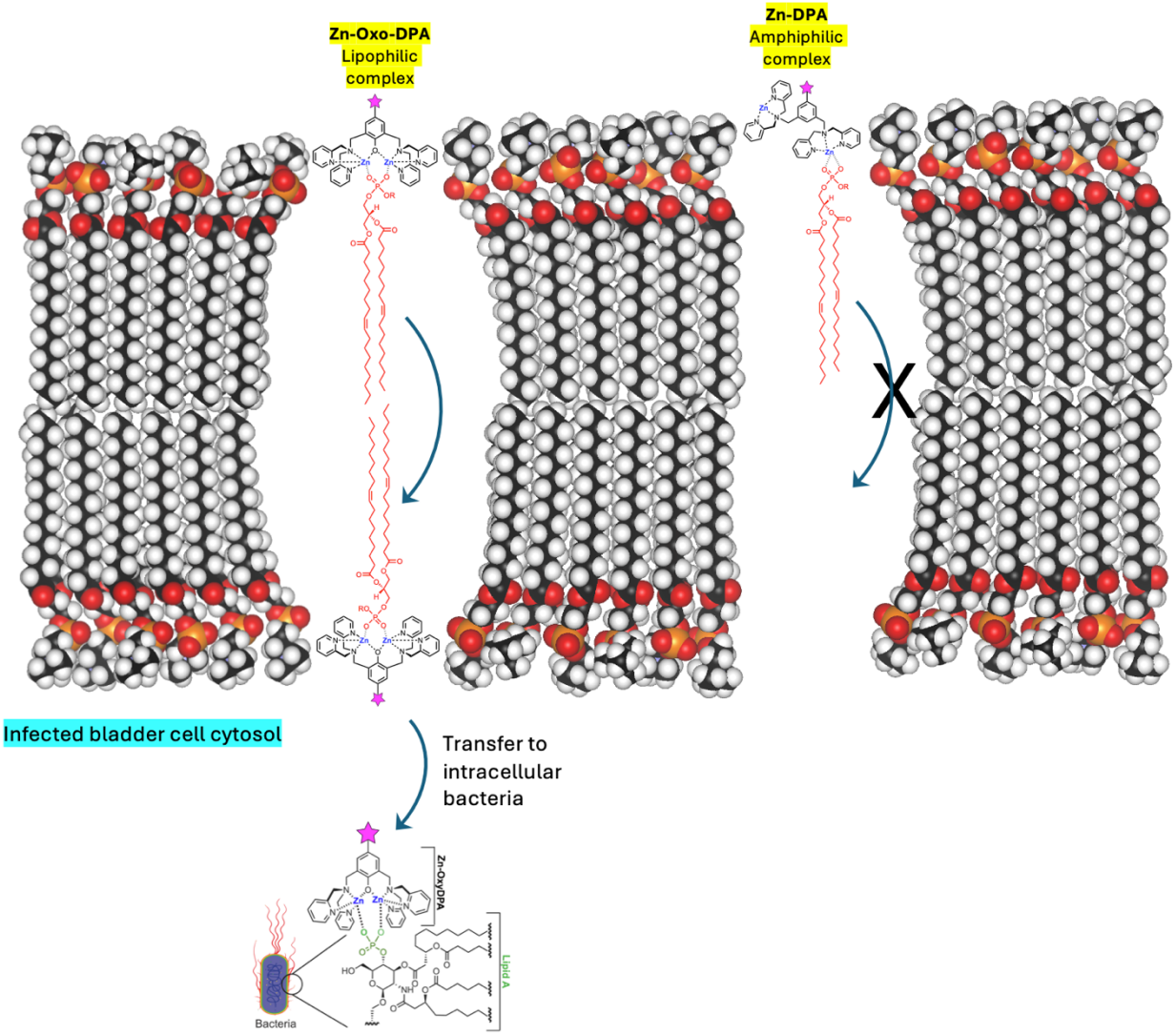

Scheme S3. (*left*) A **Zn-Oxy-DPA** targeting unit associates reversibly with a membrane polar lipid to form a lipophilic complex that diffuses through a bladder cell plasma membrane if the covalently attached dye (pink star) is charge balanced as it is in the case of **BactVue**. At the interior surface of the bladder cell membrane the **Zn-Oxy-DPA** targeting unit transfers to intracellular bacteria due to very strong binding . (*right*) A **ZnDPA** targeting unit associates with a polar lipid to form an amphiphilic complex that is relatively stable at the membrane exterior surface with a high barrier to membrane permeation. Further insight is provided by the Molecular Dynamics simulations described below.

Studies with cells and living subjects have shown that fluorescent probes with **ZnDPA** or **Zn-Oxy-DPA** targeting units strongly and selectively stain bacteria in the presence of mammalian cells.[5, 6, 13-15] The zinc affinity units associate with the anionic phosphate groups within the phospholipids that are abundant in the membrane envelope of Gram-positive bacteria (such as phosphatidyl glycerol) and the anionic glycerophosphate polymers called lipoteichoic acids that

weave through and anchor the surrounding peptidoglycan cell wall. Gram-negative bacteria have a second outer bilayer membrane. The external leaflet of this outer membrane is composed of lipopolysaccharide whose core structure, known as lipid A, contains two anionic phosphates (Scheme S4). Bacterial staining with fluorescent **ZnDPA** or **Zn-Oxy-DPA** affinity units is very strong, and the fluorescent probes are not removed by repeated washing of the bacteria.[5, 6, 13-17]

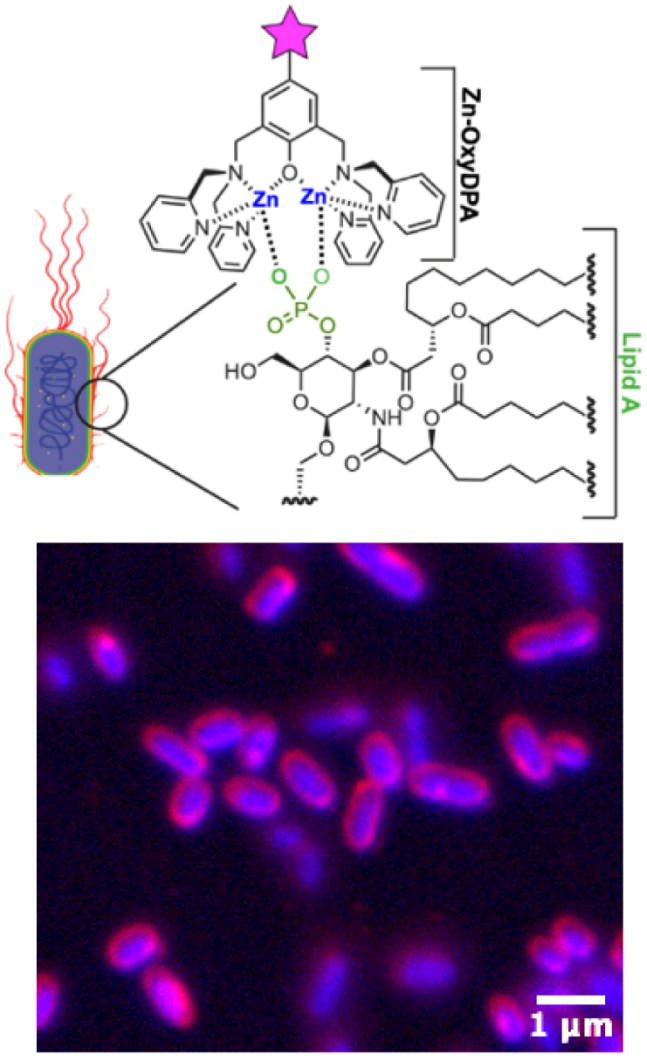

Scheme S4. Zn-Oxy-DPA binds to the phosphate groups of lipid A in the outer membrane of *E. coli*, enabling bacterial visualization. The schematic (top) illustrates the molecular interaction between **Zn-Oxy-DPA** and lipid A, demonstrating its targeting mechanism. The fluorescence image (bottom) shows *E. coli* with Hoechst-stained DNA (blue, λ_{ex} = 350 nm, λ_{em} = 461 nm) and BactVue-stained bacterial envelope (magenta, λ_{ex} = 756 nm, λ_{em} = 779 nm), confirming probe location.

In summary, **BactVue** can readily enter and exit an uninfected bladder cell (reversible permeation), but when **BactVue** enters an infected bladder cell, it strongly binds to the anionic envelope of intracellular bacteria. We also expect **BactVue** to stain any bacteria located on the bladder luminal surface, but this is not a common occurrence in a living subject that has infected bladder tissue but is urinating at regular intervals.

Materials and Methods

All chemicals were purchased from Sigma-Aldrich (St. Louis, MO), Thermo Fisher Scientific (Pittsburgh, PA), Alfa Aesar (Ward Hill, MA), TCI America (Portland, OR), VWR International (Radnor, PA), and used without further purification.

POPC, (1-palmitoyl-2-oleoyl-glycero-3-phosphocholine) and DSPE-PEG2000 [1,2-distearoyl-sn-glycero-3-phosphoethanolamine-N-[methoxy(polyethyleneglycol)2000] (ammonium salt) were purchased from Avanti Polar Lipids. Sodium chloride and chloroform were purchased from Fisher Scientific. Sodium hydroxide was purchased from Millipore Sigma. HEPES (free acid) and potassium chloride were purchased from Research Products International.

The human urinary bladder carcinoma cells 5637 used in this study were obtained from the American Type Culture Collection (Manassas, VA 20108, USA). The cells were cultured in RPMI 1640 medium with l-glutamine supplemented with 10% Fetal Bovine Serum, 1% (vol/vol) antibiotic (100 U/mL Penicillin and 0.1 mg/mL Streptomycin, Sigma-Aldrich) at 37°C in a humidified incubator with 5% CO_2. UTI89 is a uropathogenic *Escherichia coli* (UPEC) strain isolated from a patient with acute cystitis and was grown in Luria Bertani (LB) media overnight at 37°C in static conditions. *Escherichia coli* CFT703 used in this study was obtained from the American Type Culture Collection (Manassas, VA, USA). The *Enterococcus faecalis* PF13 strain was isolated from the urine of a postmenopausal woman[18], and the *Klebsiella pneumoniae* TOP52 strain was kindly provided by Dr. David A. Rosen (Washington University in St. Louis).

Instrumentation

^{1}H and ^{13}C NMR spectra were obtained using a 600 MHz Bruker Avance NMR spectrometer with residual solvent peaks as reference signals. ESI-MS were acquired using an Agilent 1100 HPLC with a PLRP-S column for separation and an ABSciex 4000 QTRAP system for detection.

Liposomes were extruded using an Avanti Mini Extruder, and DLS measurements of liposome size were taken using a Malvern Analytical Zetasizer Nano ZS. They were then pelleted using a Sorvall MX-120 micro-ultracentrifuge. Fluorescence spectra were acquired using a Biotek Synergy H4 Hybrid microplate reader.

Statistical analysis

Statistical analysis was employed with GraphPad Prism 8 software with a 99% confidence interval. The Pearson Correlation Coefficient was calculated using ImageJ software.

Movie Description:

***Nota bene**:* The supplementary movies may be identified by their file name: d4sc05680aXX, where XX is the movie number.

Movie 1: GUVs treated with BactVue. Video composed of image slices in the Cy7 channel, progressing from top to bottom.

Movie 2: GUVs treated with BactVue. Video composed of image slices in the Brightfield channel, progressing from top to bottom.

Movie 3: GUVs treated with BactVue. Video composed of image slices in merged Cy7 and Brightfield channels, progressing from top to bottom.

Movie 4: GUVs treated with BactVue. Rotating video acquired in the Cy7 channel.

Movie 5: GUVs treated with BactVue. Rotating video acquired in the Brightfield channel.

Movie 6: GUVs treated with BactVue. Rotating video acquired in merged Cy7 and Brightfield channels.

Movie 7: GUVs only. Video composed of image slices in the Brightfield channel, progressing from top to bottom.

Movie 8: GUVs only. Video composed of image slices in the Cy7 channel, progressing from top to bottom.

Movie 9: GUVs only. Rotating video acquired in the Brightfield channel.

Movie 10: GUVs only. Rotating video acquired in the Cy7 channel.

Movie 11: Simulation of membrane permeability of ZnDPA and Zn-Oxy-DPA. The movie presents a computational analysis of the membrane permeability of ZnDPA and Zn-Oxy-DPA, highlighting the dynamic interactions and transport mechanisms through a lipid bilayer.

Movie 12: Human 5637 bladder cells infected with UTI89 (GFP) and treated with Gentamicin. Then, they were treated with BactVue. After treatment with BactVue, cells were fixed, and Hoechst and WGA were added.

Movie 13: Human 5637 bladder cells infected with UTI89 (GFP) and treated with Gentamicin. Then, they were treated with BactVue. After treatment with BactVue, cells were fixed, and Hoechst and WGA were added. **The Cy7 signal was turned off**.

Movie 14: Human 5637 bladder cells infected with UTI89 (GFP) and treated with Gentamicin. Then, they were treated with BactVue. After treatment with BactVue, cells were fixed, and Hoechst and WGA were added. **The GFP signal was turned off**.

Movie 15: Human 5637 bladder cells infected with UTI89 (GFP) and treated with Gentamicin. Then, cells were fixed, and Hoechst and WGA were added. **Cells were not treated with BactVue**.

Movie 16: Human 5637 bladder cells were not infected, but they were treated with BactVue. After treatment with BactVue, cells were fixed, and Hoechst and WGA were added. **Non-infected Cells treated with BactVue**.

Movie 17: Mice were infected with UTI89 and treated with BactVue. Bladder was extracted, fixed with 4% PFA and Hoechst was added. **Infected mice bladder treated with BactVue**.

Movie 18: Mice were not infected but treated with BactVue. Bladder was extracted, fixed with 4% PFA and Hoechst was added. **Non-infected mice bladder treated with BactVue**

Absorption and emission of Anionic control dye:

Anionic control dye in water has absorption maxima at 783 nm and peak emission at 810 nm.

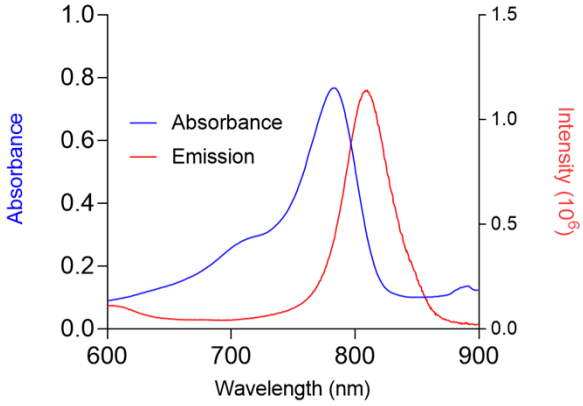

Figure S1: Absorbance and emission spectra of Anionic control ~~anionic~~ dye in water.

In vitro staining of bacteria

An aliquot of BactVue or Anionic control dye (50 µL, 0.50 mM) was added to a suspension of UTI89 bacteria (0.50 mL 0.9% saline) with an OD 0.50 and the separate mixtures were

incubated for 30 min at room temperature while rotating on a laboratory rotisserie. The samples were then centrifuged at 15,513 × g for 5 min. The bacterial pellets were collected and washed three times with 0.9% saline. Slides for microscopy were prepared and brightfield and Cy7 fluorescence micrographs were acquired using an EVOS FL digital inverted fluorescence microscope.

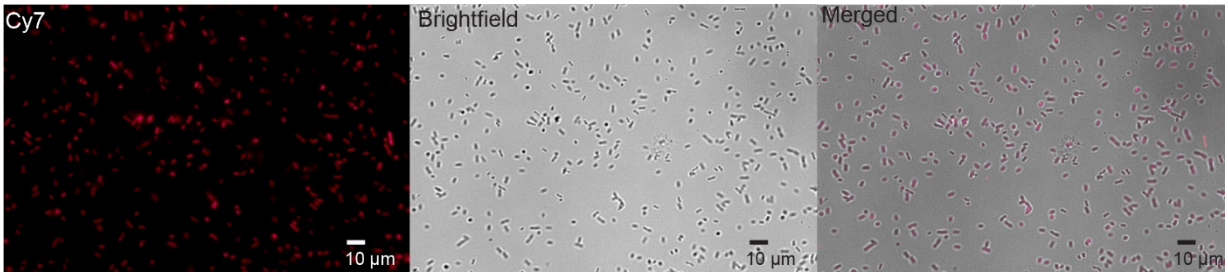

Figure S2: Cy7 fluorescence and brightfield micrographs of UTI89 bacteria stained by Anionic control dye.

In vitro staining of UTI89(GFP) bacteria

An aliquot of BactVue or Anionic control dye (50 µL, 0.50 mM) was added to a suspension of UTI89(GFP) bacteria (0.50 mL 0.9% saline) with an OD 0.50 and the separate mixtures were incubated for 30 min at room temperature while rotating on a laboratory rotisserie.

The samples were then centrifuged at 15,513 × *g* for 5 min. The bacterial pellets were collected and washed three times with 0.9% saline. Microscopy slides were prepared, and brightfield and Cy7 fluorescence micrographs were acquired using CLSM.

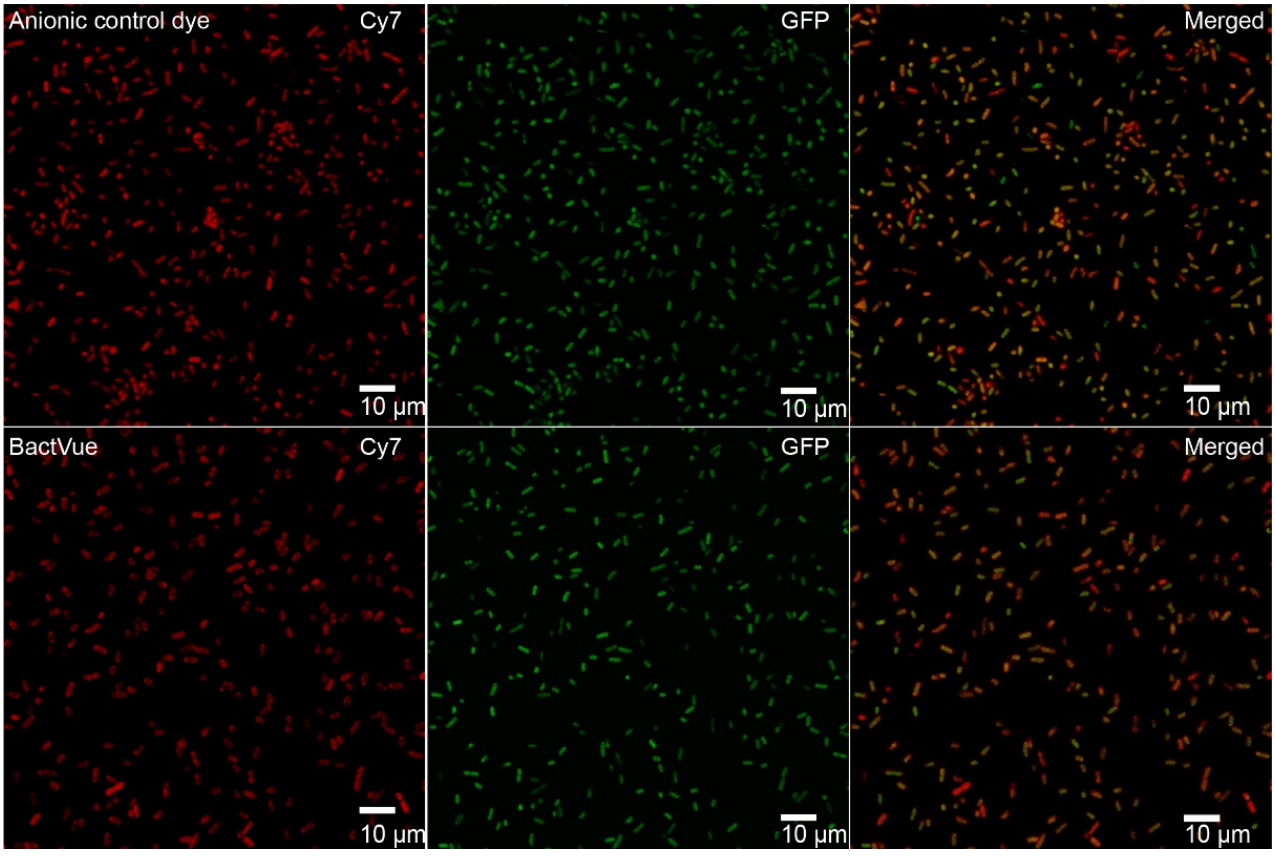

Figure S3: Cy7 and GFP fluorescence micrographs of UTI89(GFP) bacteria stained by BactVue or Anionic control dye.

Isothermal Titration Calorimetry

E. coli O26:B6 Lipopolysaccharide (LPS) (Sigma Aldrich L8274) was purchased as a lyophilized powder and made into a 10 mg/mL stock solution in 0.9% saline, and BactVue (50 mM in 0.9% saline) was used for the isothermal titration calorimetry (ITC) experiment. Expecting a relatively low affinity between BactVue and LPS, the first ITC experiment was set up with the highest LPS concentrations available. The concentrations used in the LPS Experiment 1 were too high to generate useful data for further analysis (data not shown), but the data still provided information to optimize the following experiments. In Experiments 1, 2, and 3, LPS was in the sample cell at 10, 0.65, and 1 mg/mL, respectively, while BactVue was loaded in the titration syringe at 20 mM, 350 μM, and 350 μM, respectively. ITC experiments were carried out in a Malvern PEAQ-ITC calorimeter at 20 ºC. All samples were degassed at 20 ºC for 5 min before loading into the calorimeter. In all ITC experiments, a first injection volume of 0.5 μL was employed, followed by 20 injections of 1.9 μL each, with the spacing between injections set to 120 s; all injection rates were 0.5 μL/s. The stir rate was 750 rpm, and the reference power was 5.0 μcal/s. During the acquisition, the data were processed with “adaptive filtering” in addition to the moving-average data filter with a period of 5 s. ITC data were integrated using NITPIC, the isotherms obtained from the replicated experiments of LPS were globally analyzed using SEDPHAT, and figures were rendered in GUSSI.

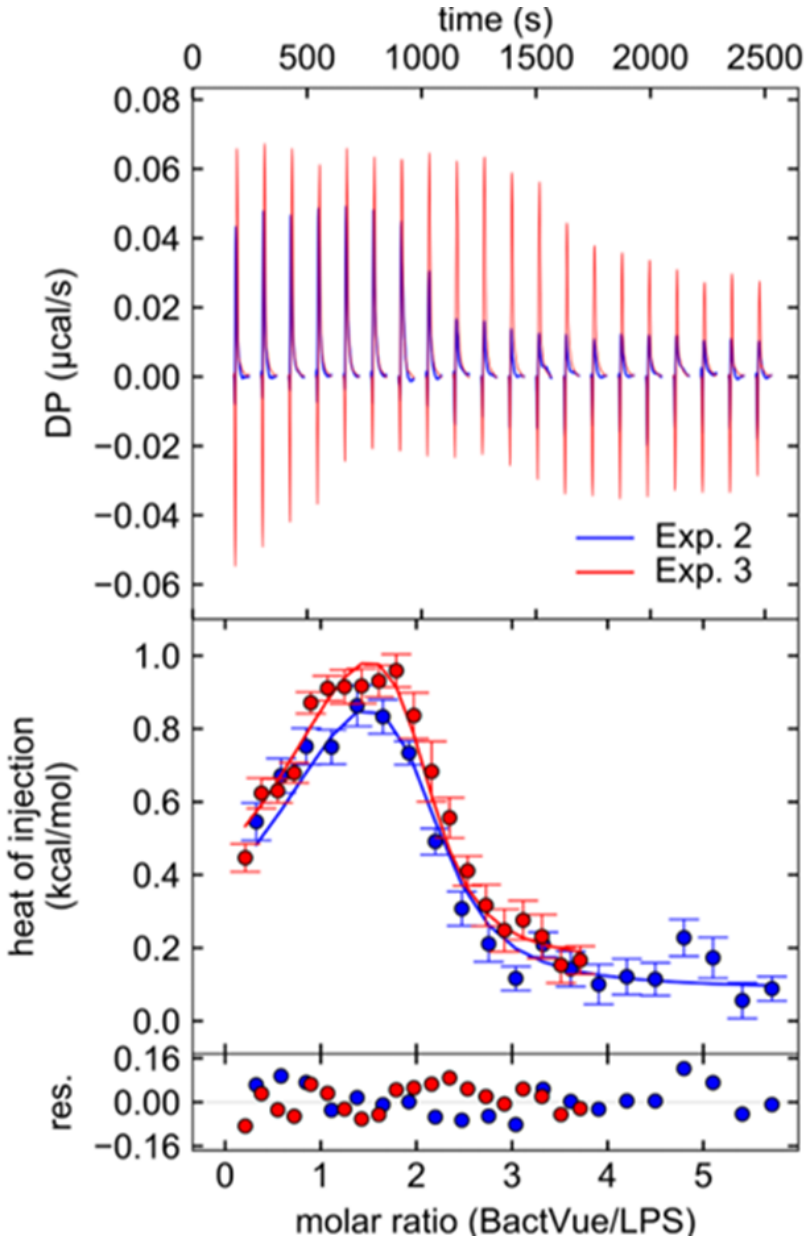

Figure S4*:* ITC results for BactVue titrated into LPS. The data sets presented in blue and red were collected in Experiments 2 and 3, respectively. The upper panel shows the SVD-corrected thermograms from NITPIC for the experiments. The middle panel displays the integrated data points with their respective estimated error bars and the fit lines obtained from global analysis. The lower panel depicts the residuals between the data and the fit line.

In vitro staining of *Escherichia coli* CFT703, *Klebsiella pneumoniae* TOP52, and *Enterococcus faecalis* PF13

The same procedure was performed separately for *E. coli* CFT703, *Klebsiella pneumoniae* TOP52, and *Enterococcus faecalis* PF13. Bacterial suspensions (0.5 mL in 0.9% saline) with an optical density (OD) of 0.50 were prepared for each strain, and 0.5 mL of Hoechst DNA dye (2 μL/mL in saline) was added to each suspension. The mixtures were incubated at room temperature for 5 min, centrifuged at 15,513 × g for 5 minutes, and the bacterial pellets were collected, washed three times with 0.9% saline, and resuspended in 0.5 mL of 0.9% saline. To each resuspended bacterial suspension, 50 μL of BactVue (0.50 mM) was added, and the mixtures were incubated at room temperature for 30 minutes. The samples were centrifuged again at 15,513 × g for 5 minutes, and the bacterial pellets were washed three times with 0.9% saline. Slides for confocal laser scanning microscopy (CLSM) imaging were then prepared using the stained bacterial suspensions, and the samples were imaged using CLSM.

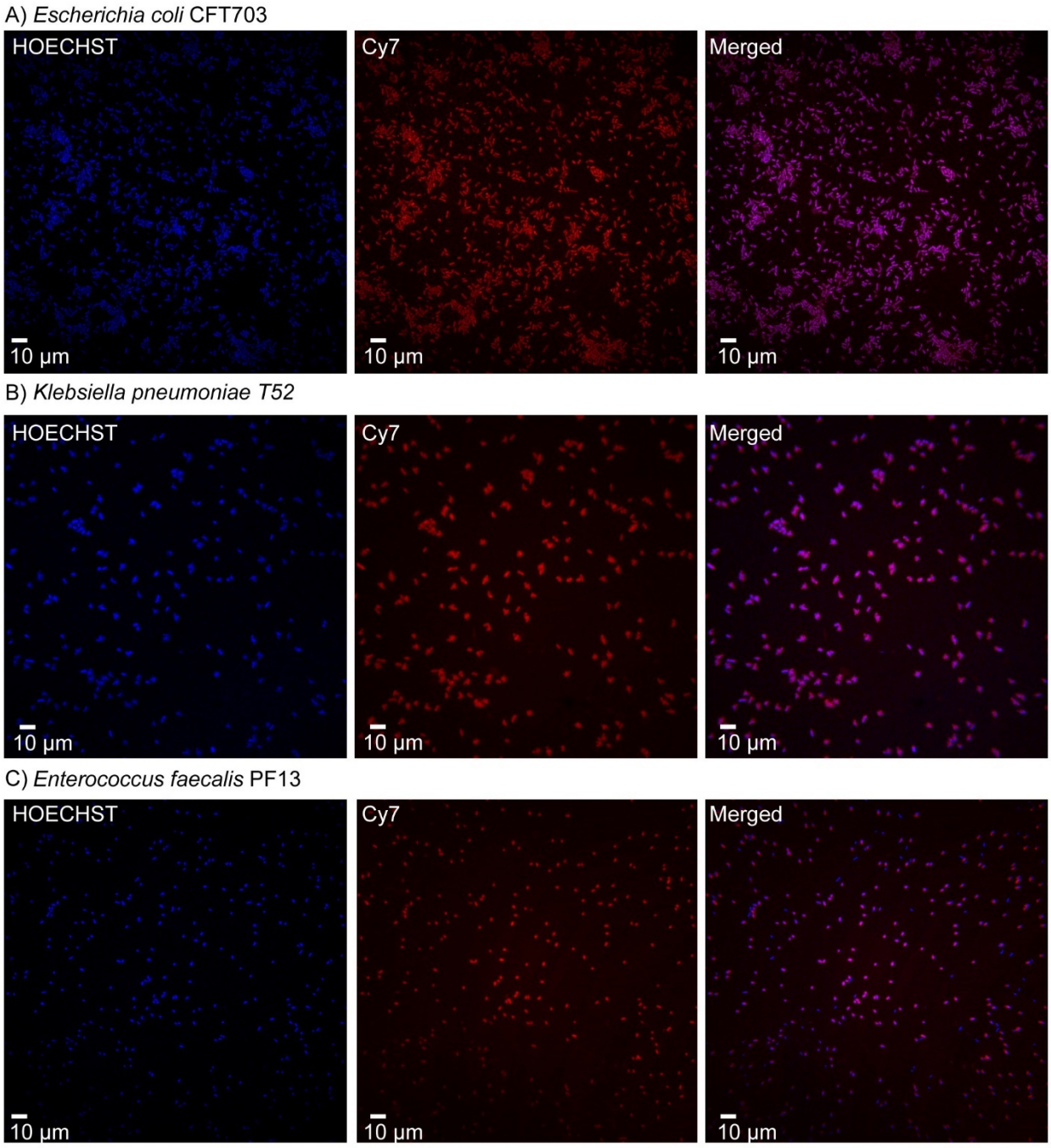

Figure S5*:* Fluorescence micrographs of *Escherichia coli* CFT703, *Klebsiella pneumoniae* T52, and *Enterococcus faecalis* PF13 bacteria stained by BactVue.

Liposome preparation

A thin film composed of POPC (24.5 mg) and 18:00 PEG2000 PE (0.50 mg) was hydrated with a 2 mL solution of 10 mM HEPES, 137 mM NaCl, and 3.2 mM KCl, pH 7.4. The suspension was subjected to five freeze-thaw cycles and then extruded serially through 1 μm, 400 nm, and 200 nm membrane filters to generate monodispersed liposomes with a diameter ~ of 250 nm.

Liposome staining

Three Eppendorf tubes were loaded with liposomes: (a) BactVue (0.20 mg), (b) Anionic control dye (0.20 mg), and (c) no probe added. After incubation at 37 °C for 2 h, the liposomes were separated from the supernatant by ultracentrifugation at 160,000 × *g* and 4 °C for 45 min. Each liposome pellet was resuspended in fresh HEPES buffer and photographed (Figure ~~S3~~S6), and a fluorescence spectrum was acquired.

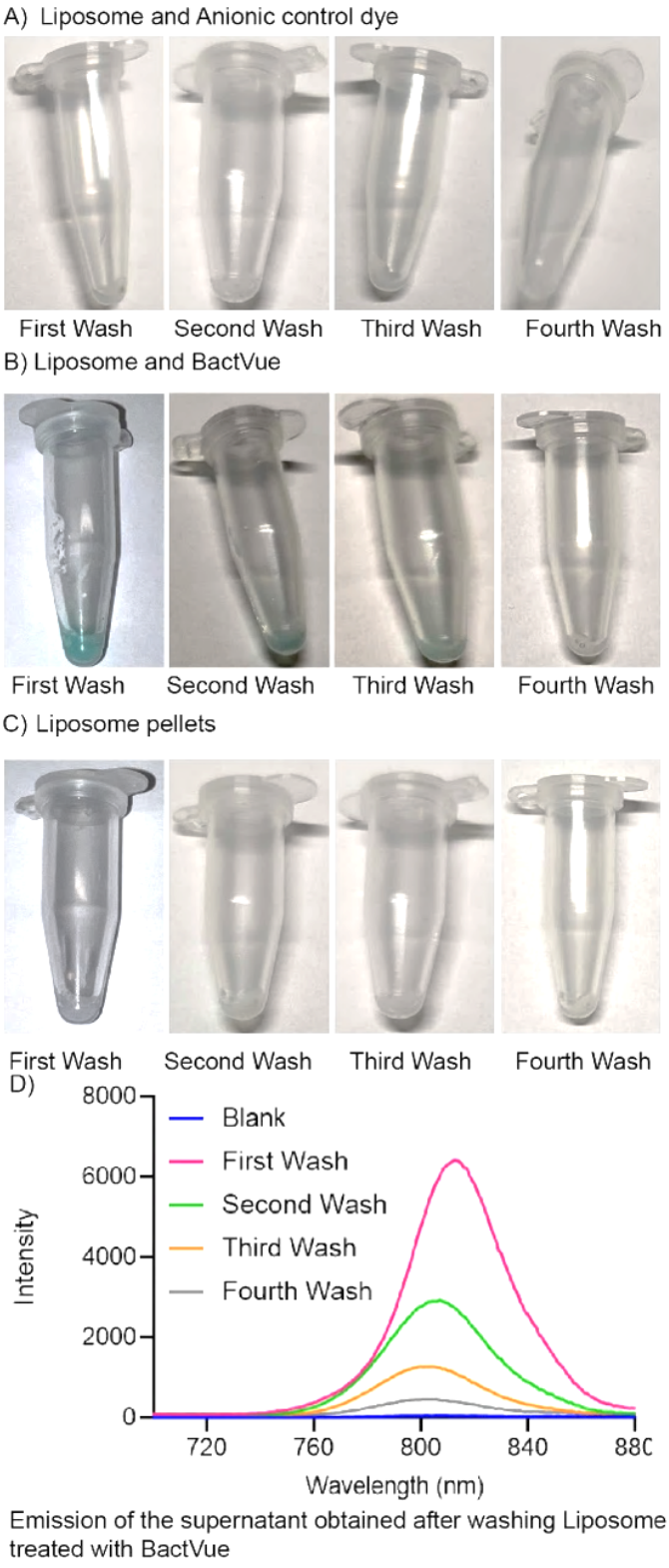

Figure S6: A) Liposomes treated with Anionic control dye in Eppendorf tubes after washes. B) Liposomes treated with BactVue in Eppendorf tubes after washing. C) Control liposomes in Eppendorf tubes after washing. D) Emission of the supernatant obtained after washing liposome treated with BactVue.

Preparation of Giant Unilamellar Vesicles (GUVs) for CLSM imaging

Electroformation chamber and setup:

The electroformation chamber was constructed using an 8-well chamber slide. Two holes were created in one of the wells, and two platinum wires (0.5 mm in diameter) were embedded near the bottom of the well. The holes were sealed using epoxy glue to ensure a tight seal. The 8-well chamber slide was chosen for its compatibility with the EVOS FL microscope, enabling real-time monitoring of GUV formation during the electroformation process.

Formation of GUVs:

Giant Unilamellar Vesicles (GUVs) are formed through a process known as AC electroformation, which involves the hydration and self-assembly of lipid molecules under an alternating electric field. In this method, a thin film of dried phospholipids is deposited onto a conductive surface, such as indium tin oxide (ITO)-coated glass or platinum electrodes. When an AC voltage is applied, the resulting oscillating electric field facilitates the hydration of the lipid film by drawing water molecules from the surrounding solution into the lipid layers, causing them to swell and reorganize into bilayers. The amphiphilic nature of phospholipids, with hydrophilic headgroups and hydrophobic tails, naturally drives the formation of these bilayers. The alternating electric field induces dipoles in the lipid molecules, leading to repulsive interactions that prevent multilayer stacking and promote the formation of unilamellar structures. Additionally, the electric field induces mechanical fluctuations in the bilayer, leading to the formation of curved regions that expand into spherical vesicles as the system seeks to minimize surface energy. These combined effects enable the efficient and reproducible production of large, uniform GUVs.

Liposomes were deposited onto each platinum (Pt) wire (10–14 drops per wire) and dried under vacuum for 30 minutes. The chamber was then sealed and rehydrated with 800 µL of 200 mM sucrose, connected to a function generator, and subjected to an AC field at 10 Hz and 2.2 V (peak-to-peak, sine wave) for 1 hour to initiate electroporation. To release the GUVs into the

solution, a detachment phase followed by reducing the frequency to 2 Hz while maintaining the same voltage for 30 minutes. A control experiment was conducted under identical conditions, substituting liposomes with HEPES buffer during deposition. The entire process was monitored using an EVOS FL microscope.

The detached GUVs were collected by pipetting the solution into a vial and mixing with 0.2 mg of BactVue, followed by incubation at 37 °C for 2 hours. A control sample containing only GUVs without BactVue was prepared in parallel. Both the sample and control were centrifuged at 15,513 × g for 5 minutes, and the supernatant was removed. The GUVs were resuspended in 1 mL of fresh HEPES buffer, repeating the washing process twice. Microscopic slides were then prepared, and CLSM imaging was performed.

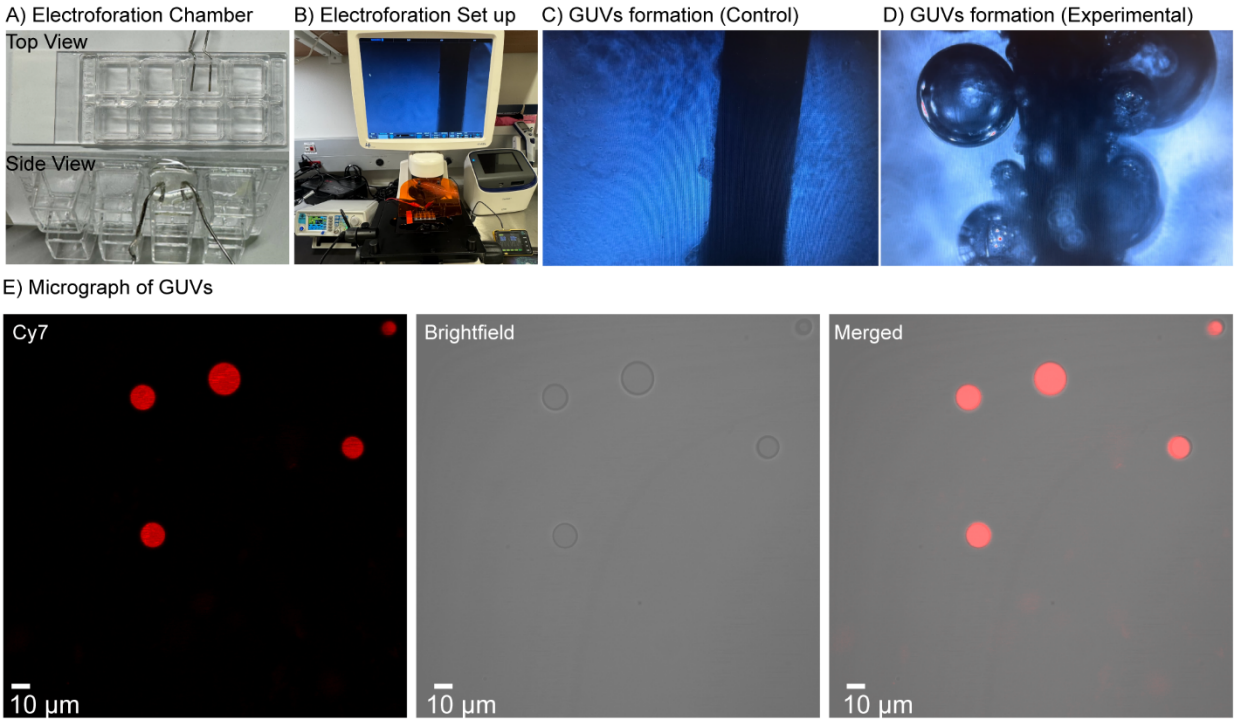

Figure S7: A) Top and side views of the electroformation chamber, constructed with platinum wires embedded in an 8-well chamber slide. B) Experimental setup for the electroformation process, showing the chamber connected to the function generator and microscope. C) Brightfield image of the platinum electrodes during electroformation with buffer only, illustrating the control condition. D) Brightfield image of the platinum electrodes during electroformation with liposome deposition, demonstrating the formation of GUVs. E) Confocal Laser Scanning Microscopy (CLSM) micrograph of Giant Unilamellar Vesicles (GUVs) treated with BactVue, confirming successful incorporation and visualization of the probe.

Computational modelling

Methods: Steered molecular dynamics simulations

To examine and compare the permeability characteristics of ZnDPA and Zn-Oxy-DPA (structures shown below), we performed steered molecular dynamics (SMD) simulations of both molecules with a mammalian asymmetric heterogeneous plasma membrane model[19]. The membrane bilayer/ligand system for the simulations was constructed using the CHARMM-GUI webserver[20]. The membrane model consists of 414 lipids, with 214 in the upper leaflet and 200 in the lower leaflet. The lipid composition of the plasma membrane is provided in Supplementary **Table S1**[19]. For ZnDPA and Zn-Oxy-DPA, the RESP charges were calculated using Gaussian16, and the charges were fitted using PARMED from AmberTools23[21, 22]. Here we used B3LYP/6-31G* level of theory for the gaussian calculations. A bonded model was used to maintain the Zn coordination in both ZnDPA and Zn-Oxy-DPA molecules. ZnDPA and Zn-Oxy-DPA molecules were placed approximately 35 Å from the center of the bilayer. Both sides of the membrane were padded with TIP3P water molecules to a distance of 30 Å[23]. Sodium and chloride ions were added to neutralize each system to a concentration of 150 mM. The initial structures were minimized for 5000 steps using the steepest descent method, followed by 15,000 steps using the conjugate gradient method. The systems were then heated from 0–100 K over 50 ps using constant volume Langevin dynamics, with lipid molecules restrained using a harmonic potential with a force constant of 10.0 kcal/mol/Å. Subsequently, the temperature was increased to 303 K over 2 ns in the isothermal-isobaric (NPT) ensemble, using the Berendsen barostat to maintain 1 bar atmospheric pressure. The force constant on the systems was reduced to 1 kcal/mol/Å. The systems were equilibrated for 10 ns with positional restraints on ZnDPA/Zn-Oxy-DPA at Z = 35 Å to keep the molecules above the membrane. After equilibration, SMD simulations were performed with a pulling rate of 0.78 Å/ns and a force constant of 5.0 kcal/mol/Å to drive the permeation of the molecules from the extracellular side to the intracellular side of the membrane in triplicates.

Trajectories were recorded every 10 ps during the SMD simulations. All simulations were conducted using the AMBER20 software package with a time step of 2 fs[24]. The Sander.MPI module was used for minimization, and the pmemd.cuda module was used for the equilibration and production simulations[24, 25]. Data analysis was performed using the cpptraj module of AmberTools23 and tcl scripts in VMD[26]. Membrane properties were calculated using MEMBPLUGIN v1.1 using VMD. Matplotlib was used for plotting, and PyMOL v3 was used for image preparation[27, 28].

Zn-Oxy-DPA is more compact than ZnDPA in membrane permeation simulations

SMD is an effective method for studying the membrane permeation of small molecules and bioorganic compounds. In our simulation, the ZnDPA and Zn-Oxy-DPA molecules were placed on the extracellular side of an asymmetric, heterogeneous mammalian plasma membrane model. A minimal force was applied to pull the molecules towards the intracellular side through the membrane. The conformational differences between ZnDPA and Zn-Oxy-DPA during membrane permeability are primarily determined by their molecular composition. In Zn-Oxy-DPA, the central oxygen atom bridges the proximal Zn ions. This oxygen –Zn ion coordination arranges the pyridine rings like the blades of a propeller and exposes part of the Zn ions, allowing them to interact with the anionic lipids in the membrane (**Figure S8A**). In contrast, in ZnDPA, the two Zn ions are positioned farther apart, exposing a larger charged surface of the Zn ions (**Figure S8A**). To analyze the effect of oxygen–Zn ion bridging, we calculated the hydrogen bonds with membrane lipids, the distance between the two Zn ions, and the surface area of the molecules **(Figure S8B)**. The number of polar interactions increases in the headgroup-interface regions of the membrane. Both ZnDPA and Zn-Oxy-DPA can form up to ten hydrogen bonds with the membrane lipids. However, Zn-Oxy-DPA shows an incremental increase in the number of hydrogen bonds at the upper leaflet interface region during membrane entry and a subsequent

incremental decrease during the exit. On the other hand, the change in ZnDPA interactions during membrane permeation does not seem to exhibit a consistent trend.

We also measured the distance between the two Zn ions within the molecules to compare the closed and open states of ZnDPA and Zn-Oxy-DPA (**Figure S8B**). In Zn-Oxy-DPA, the Zn ion distance remains constant, ranging between 2.5 Å and 3.5 Å. In ZnDPA, the distance between the Zn ions is initially 7 Å, which increases up to 9 Å, indicating that ZnDPA predominantly adopts the open conformation (**Figure S8B**). This larger distance increases the molecule's radius, which may require a larger membrane pore area to penetrate the membrane. This corroborates with the increase in the area per lipid (APL) of POPA lipids in the presence of ZnDPA **(Figure S9A)**. Both molecules have a vdW surface area between 1900-2300 Å². The surface areas of ZnDPA and Zn-Oxy-DPA are similar at the membrane entry, whereas the surface area of Zn-Oxy-DPA is ~150 Å² lower in the interface region of the lower leaflet during membrane exit compared to ZnDPA (**Figure S8B**).

Dynamics of *lipid bilayer*

To understand how the membrane responds to ZnDPA and Zn-Oxy-DPA, we studied their interactions with the membrane components. These interactions induce various structural and dynamic changes in the target membrane. We calculated several membrane properties to quantify these effects, including the area per lipid (APL), the order of the lipid acyl chains, and the membrane thickness. The area per lipid was measured to assess the compactness of the membrane. The APL of the lipid molecules is similar in the presence of molecules, except for POPA. POPA shows a drastic increase in surface area in the presence of ZnDPA, compared to Zn-Oxy-DPA. This suggests that the membrane needs to expand significantly to accommodate ZnDPA (**Figure S9A**). We then calculated the order parameter (S_{cd}) as a function of the position of the carbon atoms and the thickness of the membrane bilayer. The lipid assemblies exhibited similar behavior for both ligands (**Figures S9B, S9C**). Overall, the calculated membrane

parameters indicate that the bilayer behaves similarly with both molecules. However, the membrane is expanded during ZnDPA permeation compared to Zn-Oxy-DPA permeation.

Note: **Movie 11** compares representative simulations of membrane permeation by ZnDPA and Zn-Oxy-DPA that highlight the structural fluctuations and dynamic interactions with the membrane components.

Table S1. Molecular structures and lipid composition of mammalian plasma membrane model.

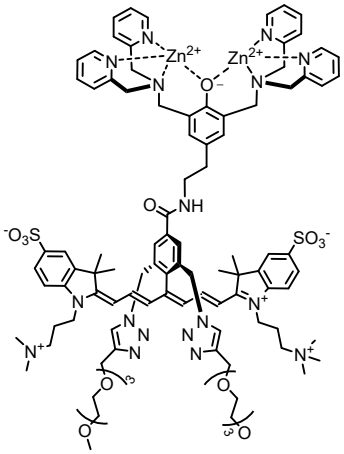

Zn-Oxy-DPA

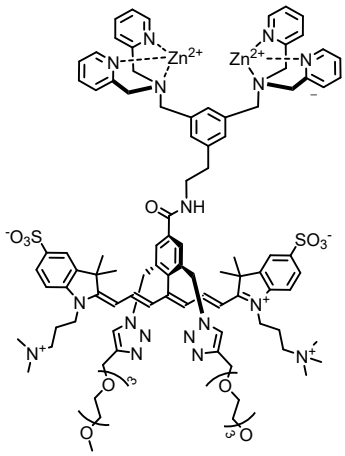

ZnDPA

Lipid	Upper leaflet	Lower leaflet
1-Palmitoyl-2-Oleoyl-sn-Glycero-3-Phosphocholine (**POPC**)	32	14
1-Palmitoyl-2-Linoleoyl-sn-Glycero-3-Phosphocholine (**PLPC**)	44	22
1-Palmitoyl-2-Arachidonoyl-sn-Glycero-3-Phosphoethanolamine (**PAPE**)	6	24
1-Palmitoyl-2-Oleoyl-sn-Glycero-3-Phosphoethanolamine (**POPE**)	6	28
1-Palmitoyl-2-Oleoyl-sn-Glycero-3-Phosphoinositol (**POPI**)	0	10
1-Palmitoyl-2-Arachidonoyl-sn-Glycero-3-Phosphoserine (**PAPS**)	0	22
1-Palmitoyl-2-Oleoyl-sn-Glycero-3-Phosphate (**POPA**)	0	2
Sphingomyelin (Saturated; typically N-Stearoyl-Sphingomyelin) (**SSM**)	22	10
Sphingomyelin (Non-Saturated; typically N-Palmitoyl-Sphingomyelin) (**NSM**)	22	10
Ceramide Monohexoside (Glucosylceramide or Galactosylceramide) (**CMH**)	8	0
Cholesterol (**CHOL**)	74	58
Total	**214**	**200**

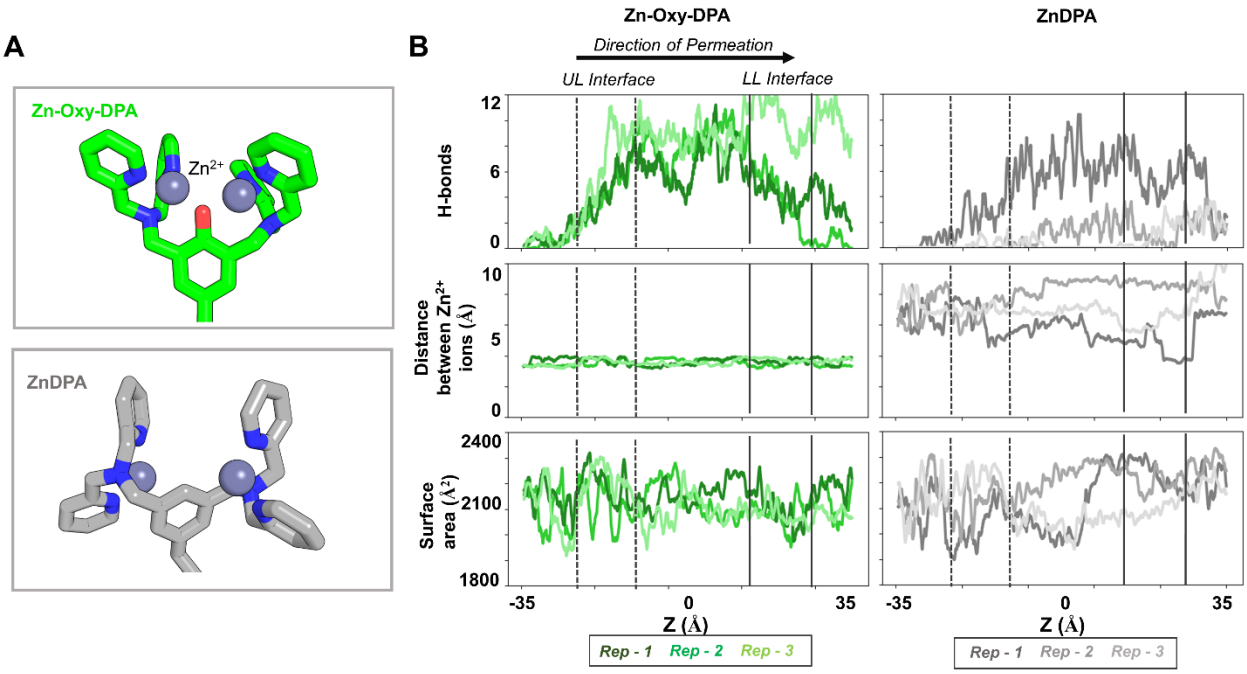

Figure S8: **Impact of oxygen–Zn ion bridging.** A) Illustrations of the Zn^{2+} coordination within Zn-Oxy-DPA and ZnDPA. B) Comparison of Zn-Oxy-DPA and ZnDPA molecular parameters during membrane permeation; number of hydrogen bonds (H-bonds) formed with membrane lipids, the distance between the two Zn ions, and the molecular surface area.

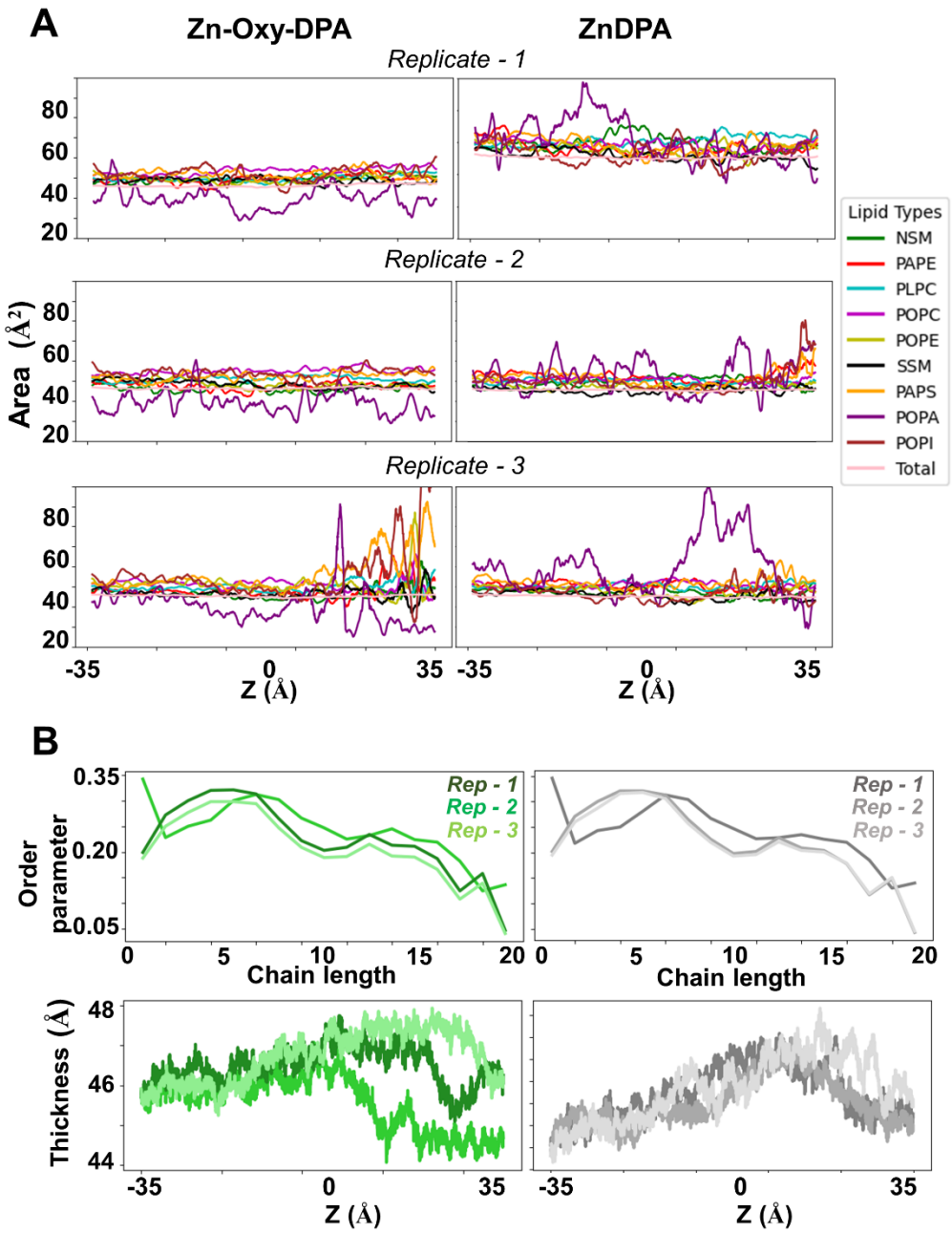

Figure S9*:* Properties of the membrane bilayer in the presence of ZnDPA and Zn-Oxy-DPA. The SMD simulations are performed by pulling the molecule from the upper leaflet (-35) towards the inner leaflet (+35). The distances are measured from the core of the bilayer (0). The data between the dashed lines and the solid lines correspond to the interface region in the membrane. A) Area per lipid (APL), showing the changes in lipid packing. B) Order parameter (S_{cd}) calculated as a function of the position of the carbon atoms in the lipid chains, indicating the effects of ZnDPA and Zn-Oxy-DPA on lipid ordering and membrane fluidity. Thickness of the membrane bilayer, illustrating the structural impact of the molecules.

Intracellular staining of UTI89(GFP) bacteria

Human 5637 bladder carcinoma cells were seeded in 6-well ~~slides~~ plates at a density of 1.5×10^5 cells/well/mL and incubated overnight at 37 °C under 5% CO_2. Following this incubation, the cells were washed three times with 0.9% saline and covered with antibiotic-free RPMI media. Next, the bladder cells were infected with bacteria by adding 20 µL of a UTI89(GFP) culture (A_{600}~0.5) to produce a multiplicity of infection (m.o.i.) of 10 bacterial cells per host cell. After a 2 h incubation period, the cell mixture was washed three times with 0.9% saline and then incubated for 2 h with 1 mL of media containing 100 µg/mL gentamicin. Another round of three saline washes was performed, followed by replacement with 1 mL antibiotic-free RPMI media. The cell mixture was treated with BactVue (final concentration of 10 µM) and allowed to incubate for 2 h followed by three saline washes. The cells were fixed by treatment with 4% paraformaldehyde at room temperature for 10 min and then subjected to two 5 min washes with 0.9% saline. To complete the staining process, 150 µL of 0.9% saline containing Hoechst (1:1000) and WGA rhodamine (1:400) was added to the cells and incubated for 10 minutes at room temperature. Two final saline washes were performed, and the microscope slides were mounted with ProLong™ Gold Antifade.

Imaging UTI89(GFP) bacteria released by lysed infected bladder cells.

Human 5637 bladder carcinoma cells were seeded in 6-well ~~slides~~ plates at a density of 1.5×10^5 cells/well/mL and incubated overnight at 37 °C under 5% CO_2. Following this incubation, the cells were washed three times with 0.9% saline and covered with antibiotic-free RPMI media. Next, the bladder cells were infected with bacteria by adding 20 µL of a UTI89(GFP) culture (A_{600}~0.5) to produce a multiplicity of infection (m.o.i.) of 10 bacterial cells per host cell. After a 2 h incubation period, the cell mixture was washed three times with 0.9% saline and then incubated for 2 h with 1 mL of media containing 100 µg/mL gentamicin. Another round of three saline washes was performed, followed by replacement with 1 mL antibiotic-free RPMI media. The cell mixture was treated with BactVue or Anionic control dye (final concentration of 10 µM) and allowed to

incubate for 2 h followed by three saline washes. The bladder cells were lysed by treatment with 0.1% triton X 100, and the samples were centrifuged at 15,513 ×*g* for 5 min. The released UTI89(GFP) cells were collected as a pellet and loaded to slides for brightfield and fluorescence microscopy.

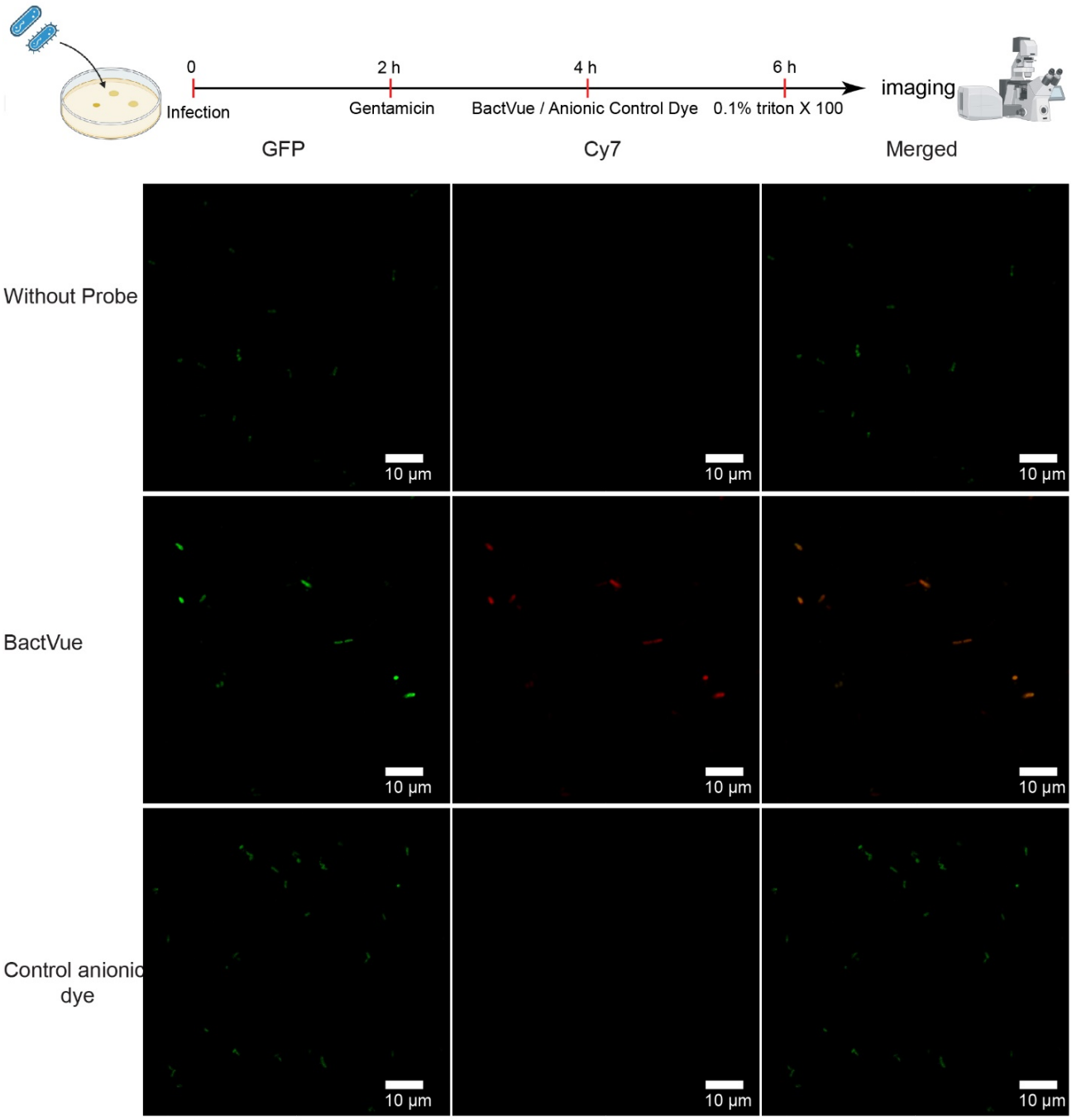

Figure S10: Fluorescence and brightfield micrographs of UTI89(GFP) bacteria released by lysed infected bladder cells that had been treated by BactVue or Anionic control dye. The bacteria were stained by BactVue but not by the Anionic control dye.

Bladder CFU measurement from acute UTI model.

Nine BALB/c mice were grouped into three groups (n = 3): Group A (infected with UTI89 and injected with BactVue), Group B (injected with BactVue only), and Group C (infected with UTI89 only). Mice in Groups A and C were infected with 50 µL of 1×10^7 CFU UTI89 suspension via transurethral inoculation and were subsequently incubated for 24 h as described previously.[29] After this incubation period, mice in Group A (24 h post-infection) and Group B were injected with 50 µL of 50 µM BactVue intravesically. *In vivo* fluorescence monitoring continued until Group B (injected with BactVue only) exhibited fluorescence, typically taking 3 h; meanwhile, Group A showed a significant fluorescence. Following 3 h of *in vivo* imaging, all mice were sacrificed, and their bladders were excised for *ex-vivo* imaging. After ex-vivo imaging, the bladders were homogenized in a lysing matrix tube containing 800 µL of PBS. The resulting suspension was then passed through 20G and 25G syringes. Subsequently, the suspension was serially diluted into seven dilutions and plated on CHROMagar culture plates. These plates were incubated at 37°C for 8 h and colony counting was performed to determine CFU.

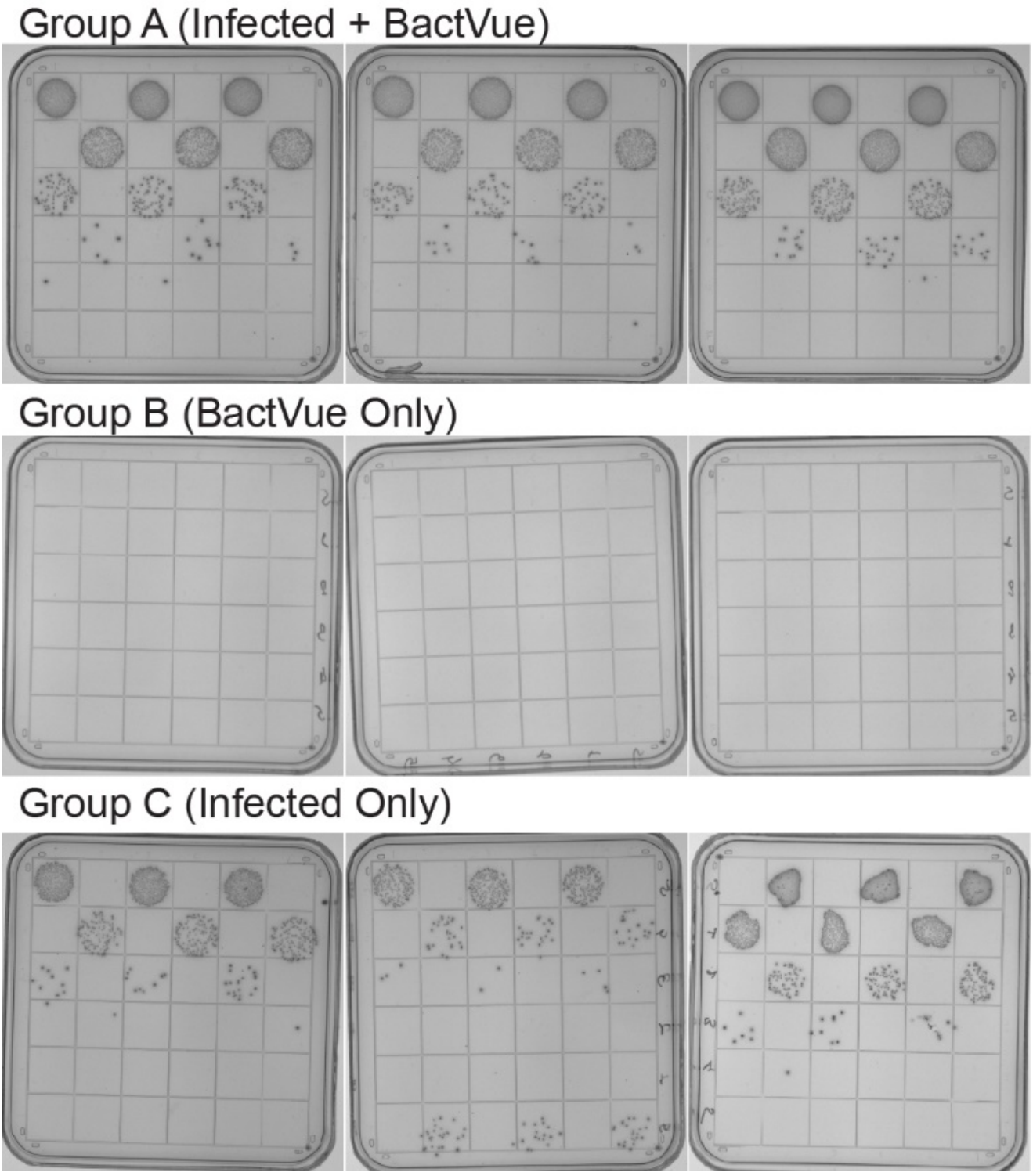

Figure S11: Bacterial colony count on CHROMagar culture plates.

In vivo, fluorescence imaging with BactVue administrated via intravesical injection

All animal studies adhered to protocol #19-06, which was approved by the University of Texas at Dallas Institutional Animal Care and Use Committee (IACUC). Nine female BALB/c mice (Charles River Lab, Wilmington, MA) were divided into three groups (each N = 3): Group A (infected with UTI89 and injected with BactVue), Group B (injected with BactVue only), and Group C (infected with UTI89 only). The mice in Groups A and C were infected with 50 μL of 1×10^7 CFU of UTI89 via intravesical injection and incubated for 24 h. The mice in Group A (after the 24 h incubation) and the mice in Group B were injected with 50 μL of 50 μM BactVue and imaged using a commercial in vivo imaging station (IVIS Lumina III) with the following instrument settings: Excitation: 740 nm, Emission: 790 nm, Exposure time: 2 s, F-stop: 1, FOV: 24 (with lens), Binning: Low.

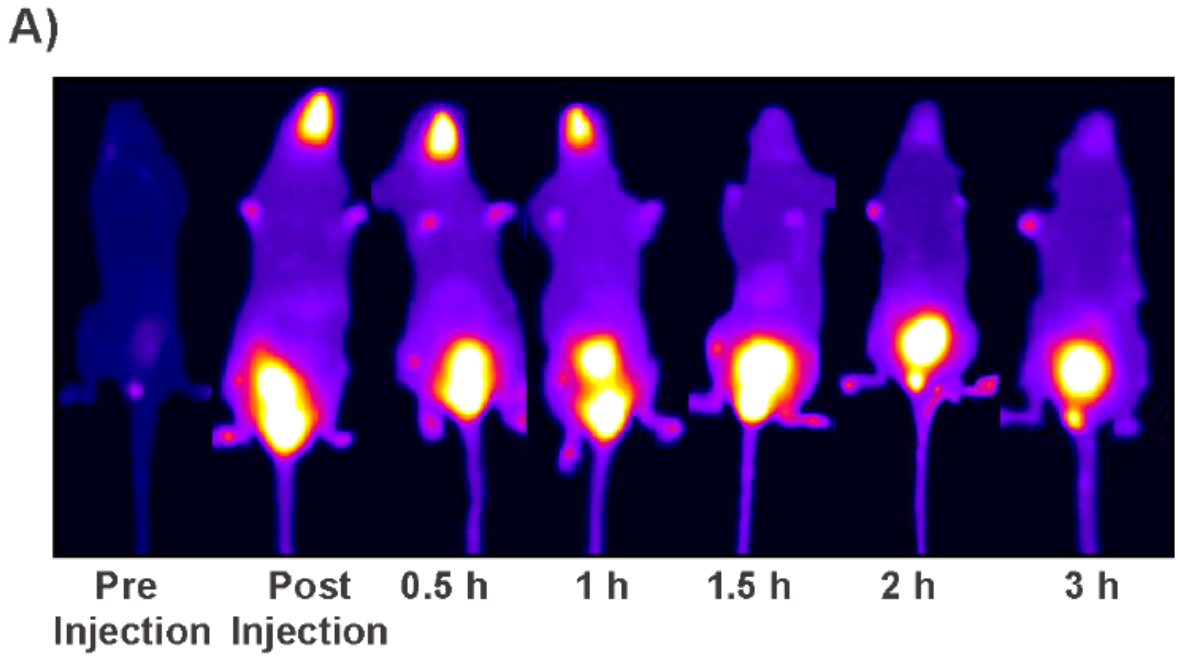

Figure S12: Representative in vivo fluorescence imaging. A) Group A mouse, bladder infected with UTI89 bacteria and injected with BactVue. B) Group B non-infected mouse, bladder injected with BactVue (ex/ 740nm and em/ 790nm).

In vivo, fluorescence imaging with BactVue administrated via tail vein injection

Six female BALB/c mice (Charles River Lab, Wilmington, Ma) were divided into two groups (each N = 3), Group A (infected with UTI89 and injected with BactVue), and Group B (Injected with BactVue only). Group A mice were infected with 50 µL of 1×10^7 CFU of UTI89 via intravesical injection and incubated for 24 h. The group A mice (after the 24 h incubation) and group B mice were injected with 50 µL of 50 µM BactVue via tail vein injection and imaged using a commercial in vivo imaging station (IVIS Lumina III) with the following instrument settings, Excitation: 740 nm, Emission: 790 nm, Exposure time: 2 s, F-stop: 1, FOV: 24 (with lens), Binning: Low.

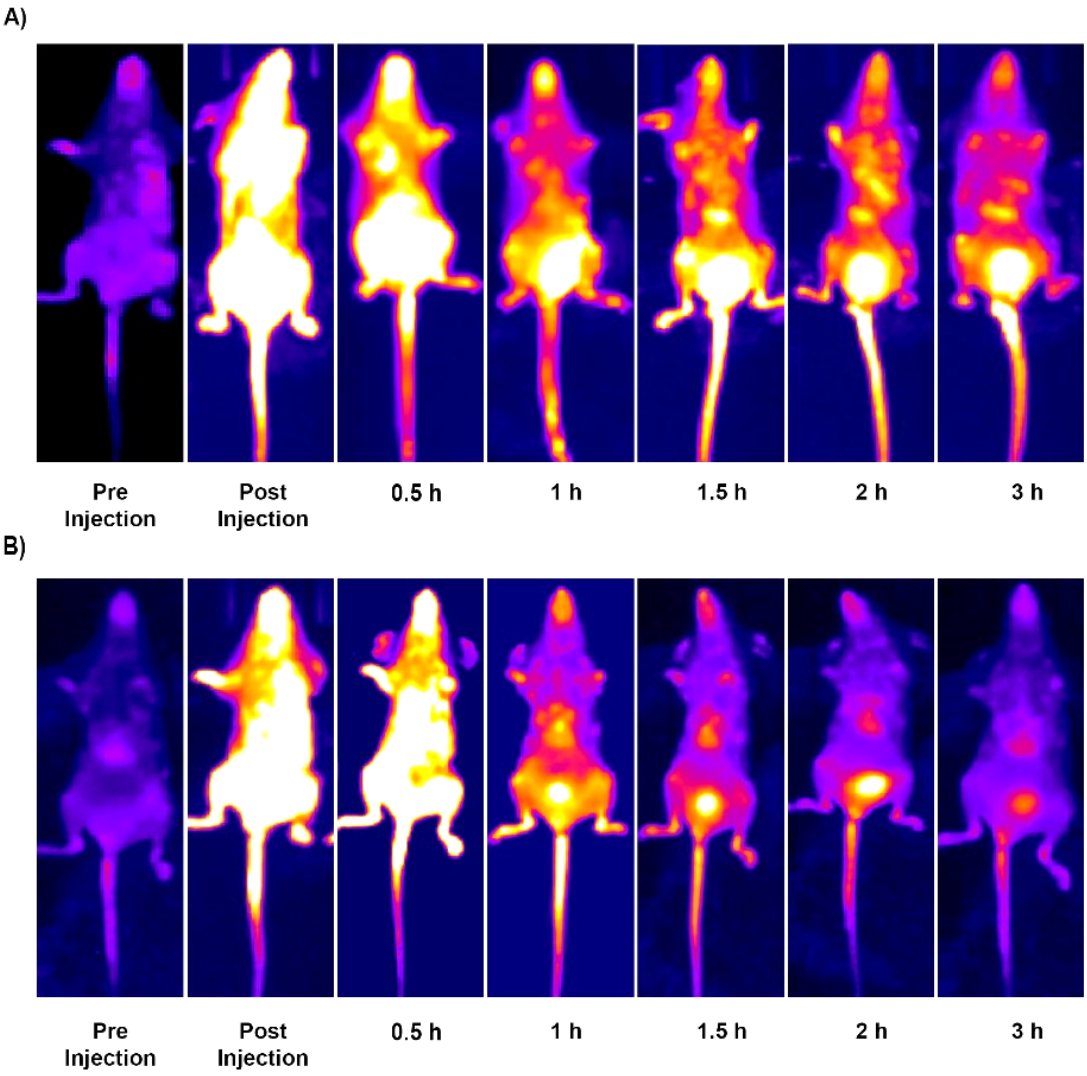

Figure S13: Representative *in vivo* fluorescence imaging. A) Group A mouse, bladder infected with UTI89 bacteria and mouse injected with BactVue via tail vein. B) Group B non-infected mouse, mouse injected with BactVue via tail vein (ex/ 740nm and em/ 790nm).

Ex-vivo fluorescence imaging

After 3 h of *in vivo* imaging, all the mice were sacrificed, bladders were excised, and imaged using a commercial in vivo imaging station (IVIS Lumina III) with the following instrument settings, Excitation: 740 nm, Emission: 790 nm, Exposure time: 3 s, F-stop: 1, FOV: 12.5, Binning: Low. After *ex-vivo* imaging, each bladder was placed in a lysing matrix tube containing 800 µL PBS and homogenized. The resulting suspension was passed through a 20 G, and 25 G syringe, then diluted by different factors and plated on CHROMagar culture plates. The culture plates were incubated at 37 °C for 8 h and the colony number counted using AlphaImager HP to determine CFU/mL.

Ex-vivo bladder confocal microscopy.

Two groups of female BALB/c mice (each n = 3), were utilized in this experiment, a non-infected control group and a UTI89-infected group. The UTI89-infected mice were subjected to intravesical injection with 50 µL of UTI89 bacteria at a concentration of 1×10^7 CFU. After a 24 h incubation, both groups of mice were given an intravesical injection of 50 µL of BactVue at a concentration of 50 µM. After a 3 h incubation, the mice were sacrificed, and their bladders were extracted. The bladders were bisected longitudinally and stretched on an agar bed, secured with pins and with the luminal side facing up. Each bladder tissue was fixed by adding 1 mL of 4% paraformaldehyde and incubating for 45 min at room temperature. After washing each bladder three times with 0.9 % saline, an aliquot of 1 mL of saline containing Hoechst (1:1000) was added and incubated for 10 min at room temperature. The bladders were washed three times with 0.9% saline to remove any excess Hoechst stain. Finally, microscopic slides were prepared for CLSM imaging by mounting the bladders along with ProLong™ Gold Antifade. Excitation and emission wavelengths for Hoechst were 350 nm and 461 nm; for GFP 395 nm and 509 nm; for WGA rhodamine 570 nm and 590 nm; and for Cy7 were 756 nm and 779 nm.

Limit of detection (LOD) for BactVue:

A solution of BactVue (20 μM) was added to a bacterial suspension of UTI89 (3 × 10^8 CFU/mL). The mixture was incubated at 37 °C for 30 min, followed by centrifugation at 15,513 × g for 5 min. The pellet was washed twice with buffer and resuspended. Serial dilutions (10-fold) were prepared down to 3 × 10^5 CFU/mL. Emission spectra were recorded, and the emission maximum was observed at 810 nm, corresponding to the known emission maxima of BactVue. A fluorescence intensity vs. CFU/mL graph was plotted to determine the limit of detection (LOD) for BactVue.

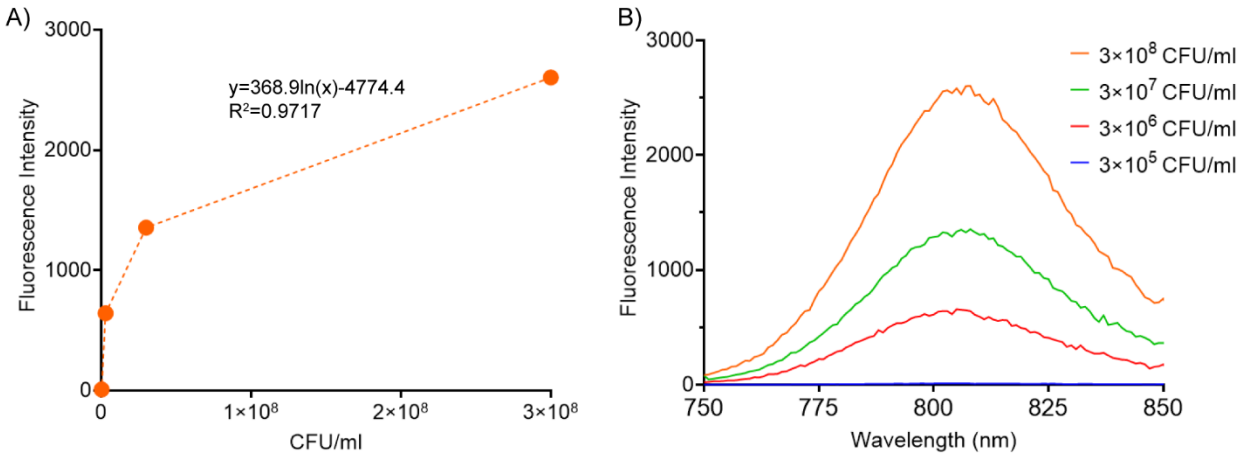

Figure S14: A) Fluorescence intensity vs. UTI89 concentration. B) Fluorescence intensity vs wavelength.

Synthesis

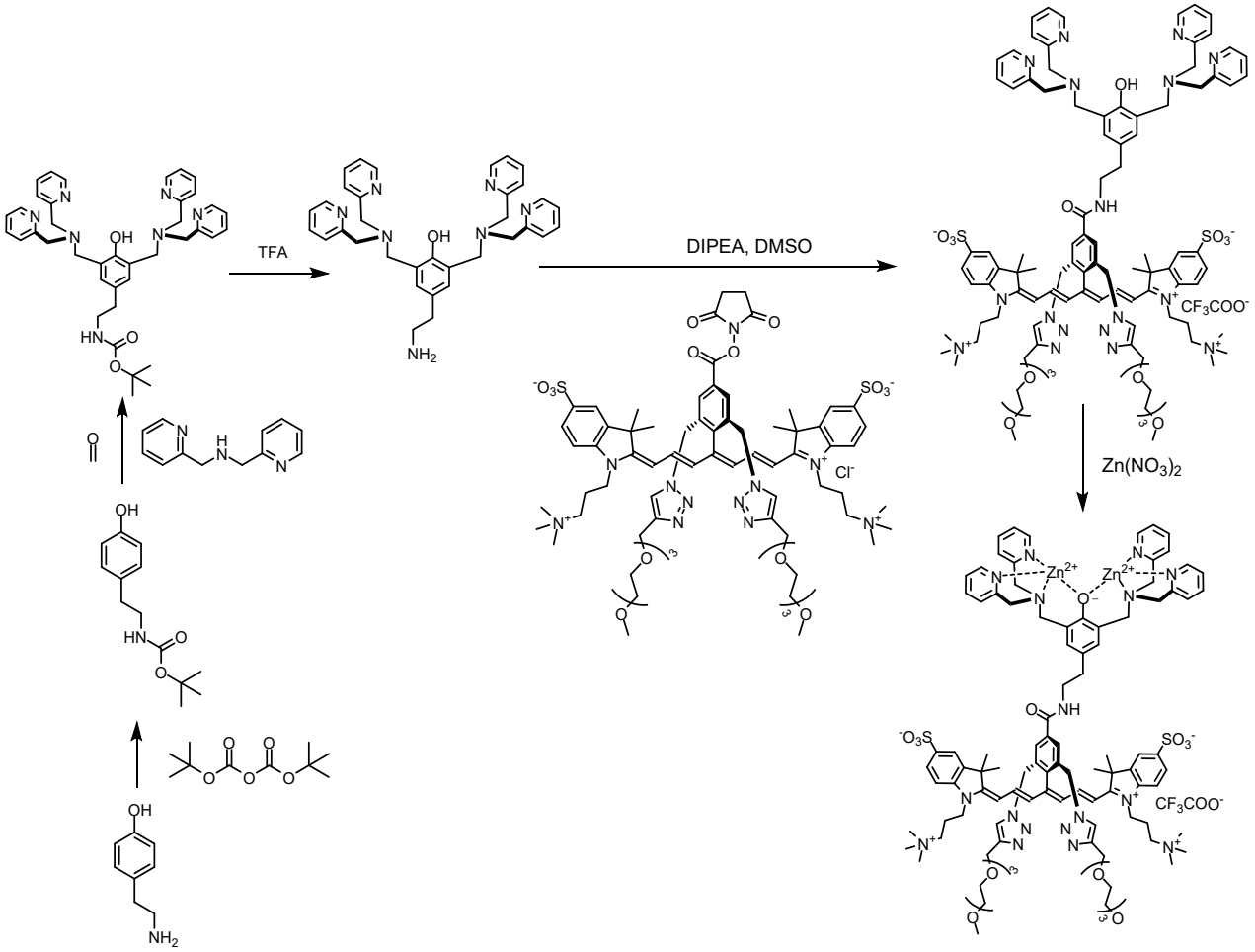

Scheme S5: Synthesis of BactVue.

Synthesis of BactVue:

Synthesis of tert-butyl(4-hydroxyphenethyl) carbamate (N-Boc-tyramine)

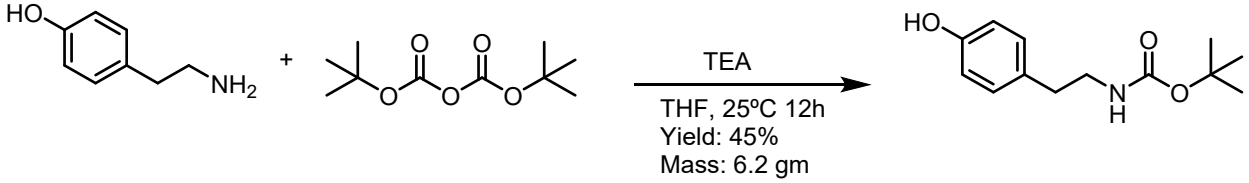

N-Boc-tyramine, tyramine (8.00 g, 58.31 mmol), di-tert-butyl dicarbonate (12.72 g, 58.28 mmol) and triethylamine (5.89 g, 58.28 mmol), were dissolved in 100 mL solutions of THF and was stirred

for 12 h at RT. The solvent was evaporated under reduced pressure and the residue was further purified by silica chromatography (gradient 0-20 % Ethyl acetate in hexane) to yield a white solid. (6.20 g, 45%) ^{1}H NMR (600 MHz, CDCl3) δ 7.02 (d, J = 7.60 Hz, 2H), 6.77 (dd, J = 1195.80, 90.50 Hz, 2H), 3.33 (q, J = 6.80 Hz, 2H), 2.71 (t, J = 7.3 Hz, 2H), 1.44 (s, 9H).

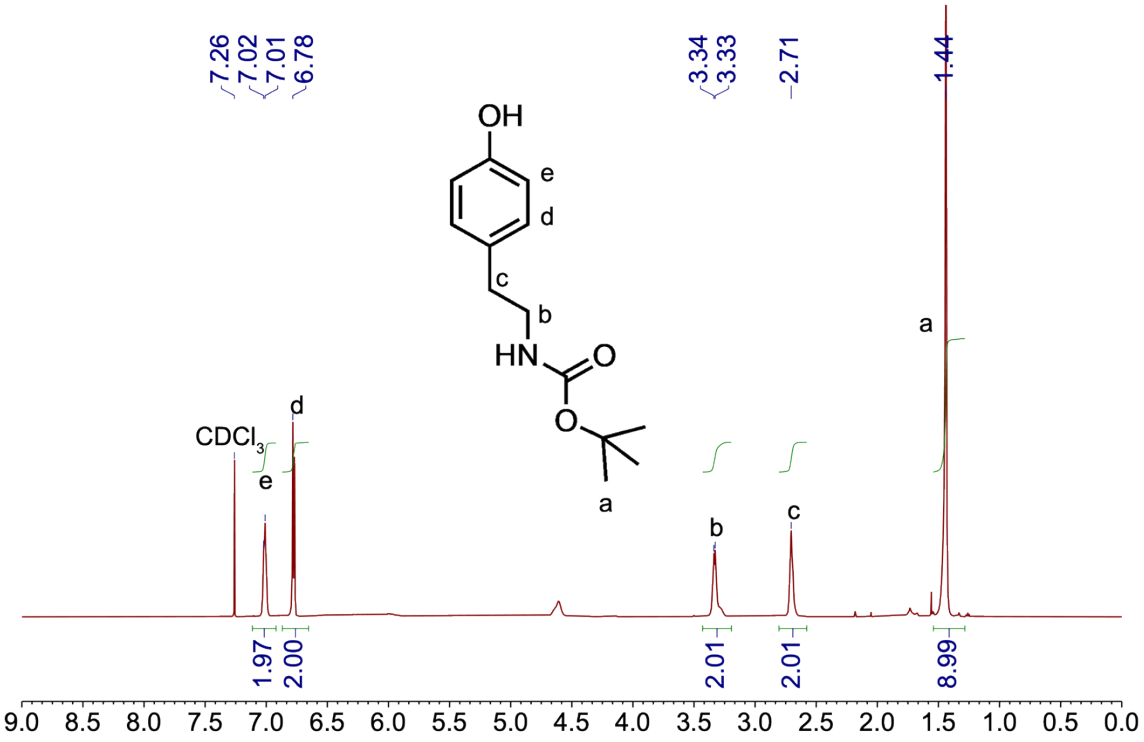

Figure S15: ^{1}H NMR of tert-butyl (4-hydroxyphenethyl) carbamate.

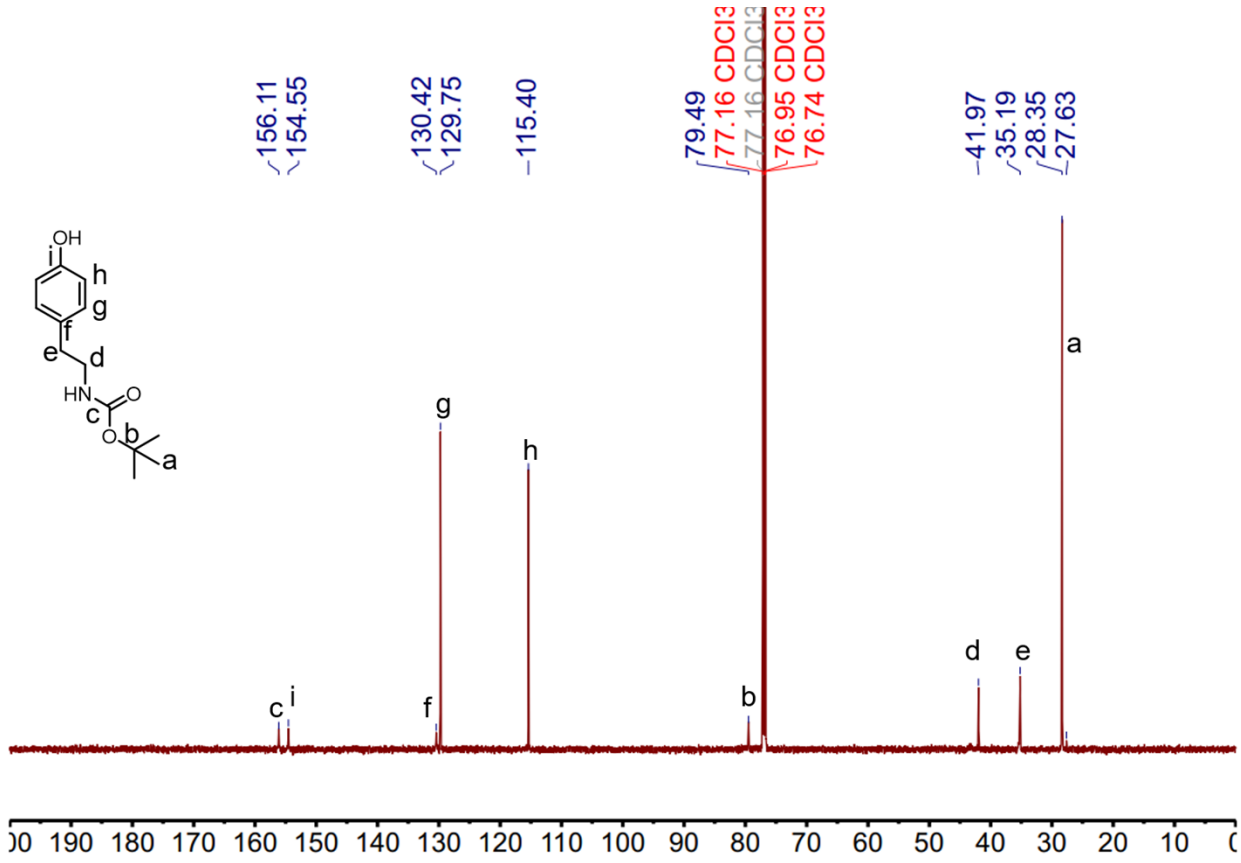

Figure S16: ^{13}C NMR of tert-butyl (4-hydroxyphenethyl) carbamate.

Synthesis of tert-butyl (3,5-bis((bis(pyridin-2-ylmethyl) amino)methyl)-4-hydroxyphenethyl)carbamate (1)

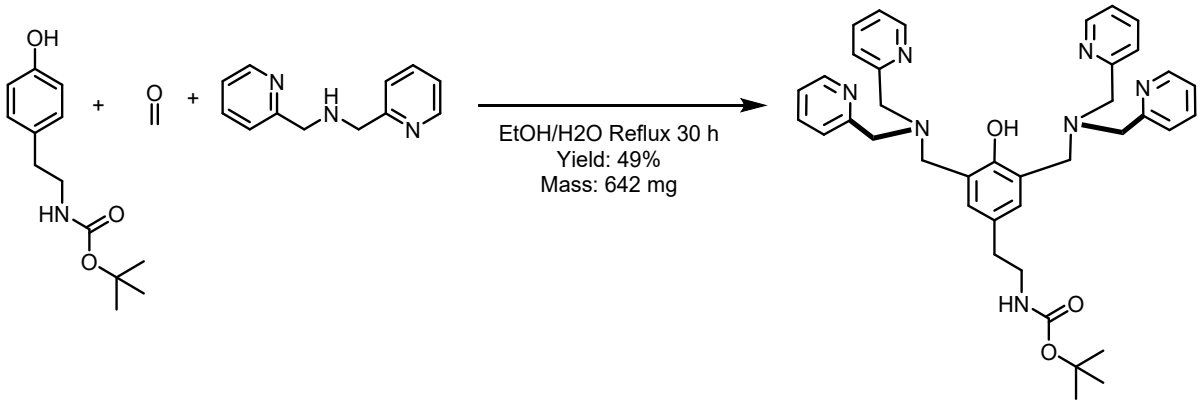

N-Boc-tyramine (474.28 mg, 2.00 mmol), paraformaldehyde (150.13 mg, 2.00 mmol), and bis(pyridin-2-ylmethyl) amine (876.70 mg, 4.40 mmol), were dissolved in 50 mL solutions of

ethanol and water (5:1 ratio) and was refluxed for 30 h. The solvent was evaporated under reduced pressure, dissolved in 25 mL DCM, and washed with H_2O 3×. The organic fraction was purified by silica chromatography (gradient 0-20 % Methanol in DCM) to yield **1** as a yellow oil. (642 mg, 49%). ^{1}H NMR (400 MHz, CDCl3, 25°C) δ 10.87 (s, 1H), 8.44 (d, 4H), 7.51 (td, 4H), 7.41 (d, 4H), 7.03 (td, 4H), 6.94 (s, 2H), 4.81 (t, 1H), 3.78 (s, 8H), 3.70 (s, 4H), 3.25 (q, 2H), 2.61 (t, 2H), 1.31 (s, 9H).

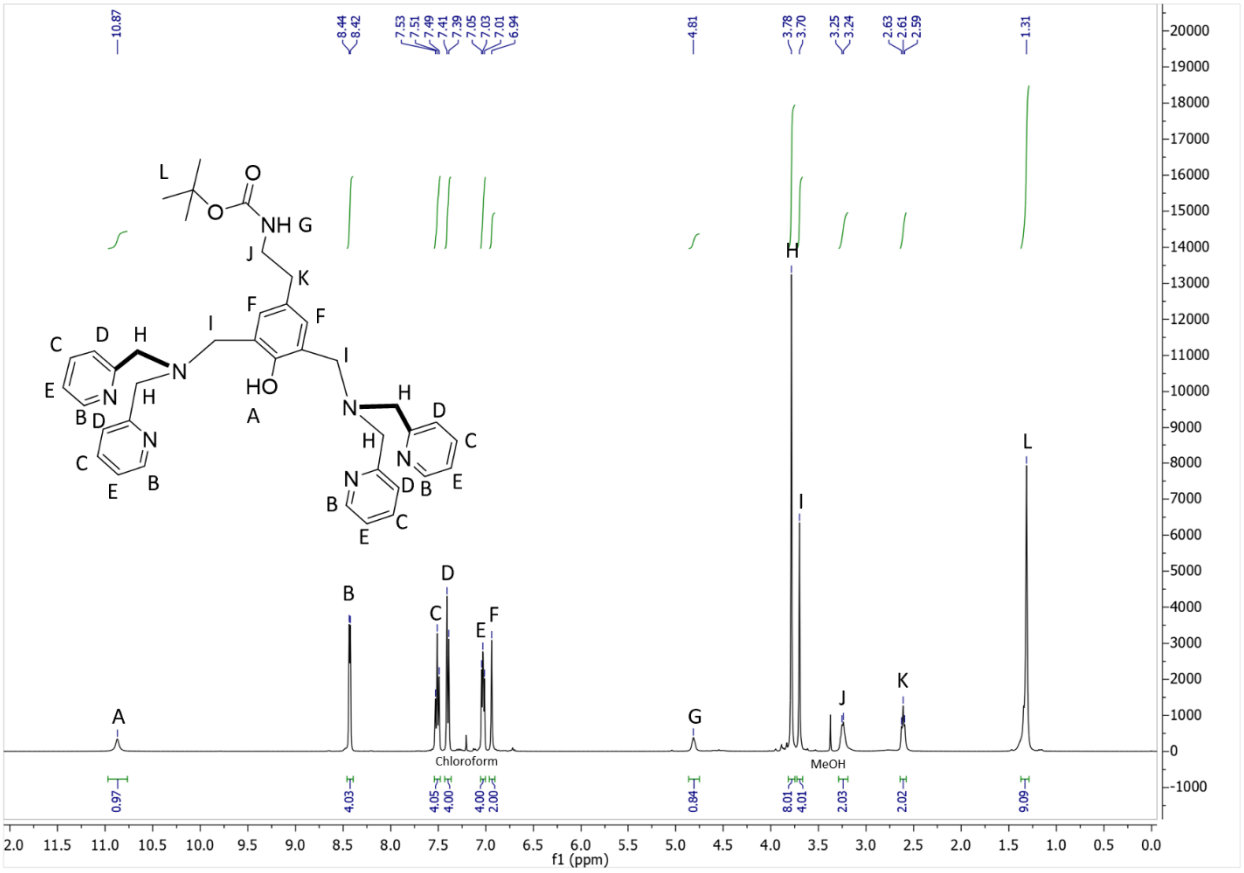

Figure S17: ^{1}H NMR of tert-butyl (3,5-bis((bis(pyridin-2-ylmethyl) amino)methyl)-4 hydroxyphenethyl)carbamate (1).

Synthesis of 4-(2-aminoethyl)-2,6-bis((bis(pyridin-2-ylmethyl) amino) methyl)phenol (2)

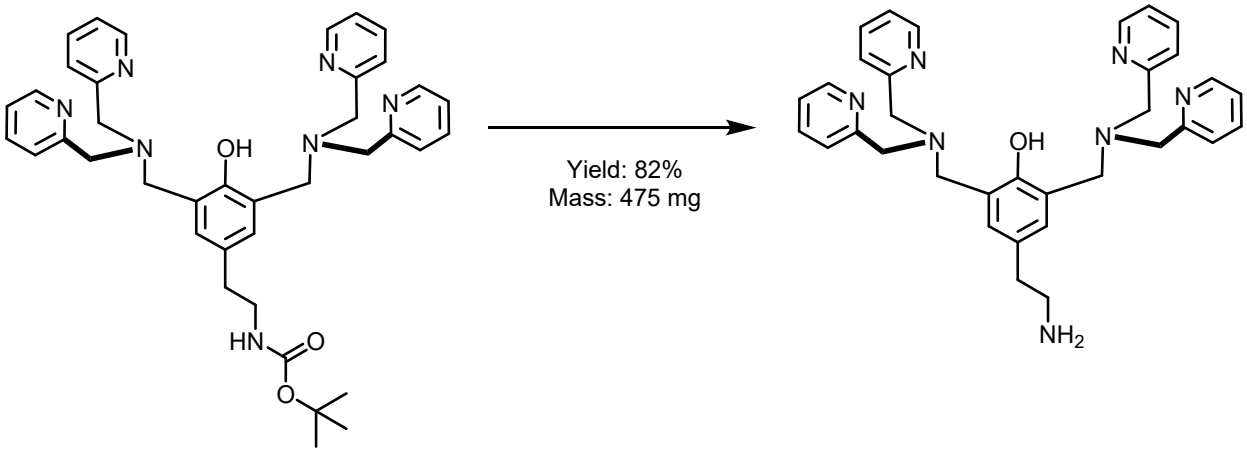

Compound **1** (642 mg, 2.50 mmol) was dissolved into 20 mL of a mixture of DCM/trifluoroacetic acid (TFA) (1:1), and the solution was stirred at room temperature for 1 h. The solvent was evaporated under reduced pressure to yield **2** as a yellow oil (0.48 g, 82%). ^{1}H NMR (600 MHz, D_2O) δ 8.61 (d, J = 5.90 Hz, 4H), 8.40 (td, J = 8.10, 2.10 Hz, 4H), 7.98 – 7.76 (m, 8H), 6.91 – 6.78 (m, 2H), 6.48 (dd, J = 8.40, 1.90 Hz, 2H), 4.40 (s, 8H), 3.71 (d, J = 2.20 Hz, 4H), 3.09 (d, J = 7.70 Hz, 2H), 2.73 (d, J = 7.70 Hz, 2H). MS (ESI-positive) Expected m/z=560.31, Found m/z = 560.40 [M^+H^+], m/z = 582.24 [M^+Na^+].

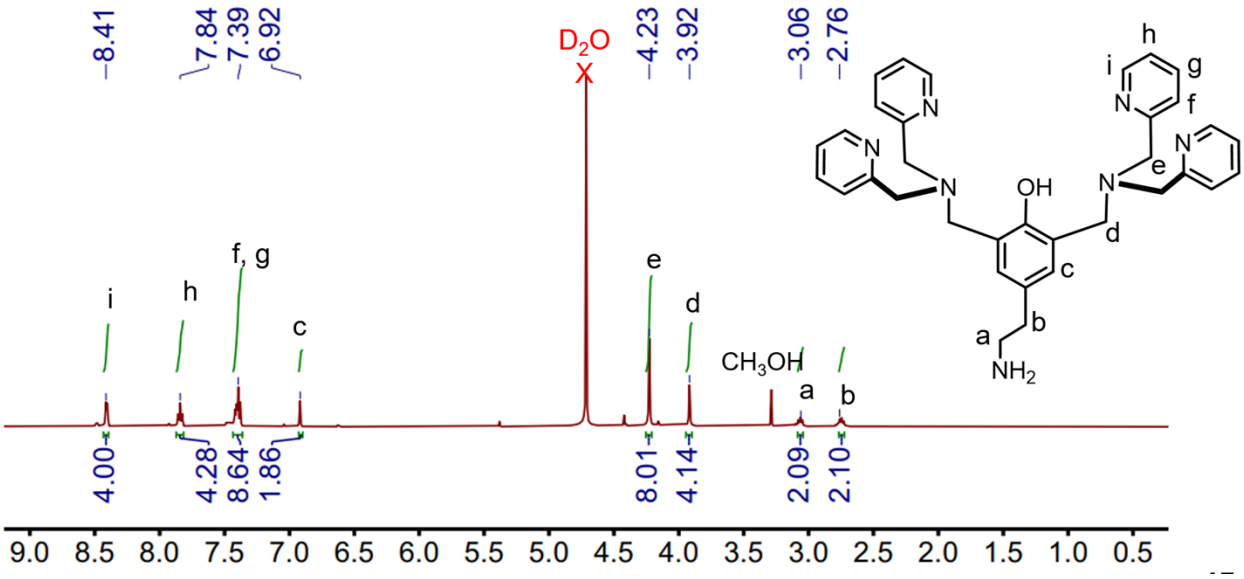

Figure S18: ^{1}H NMR of 4-(2-aminoethyl)-2,6-bis((bis(pyridin-2-ylmethyl) amino) methyl) phenol (2).

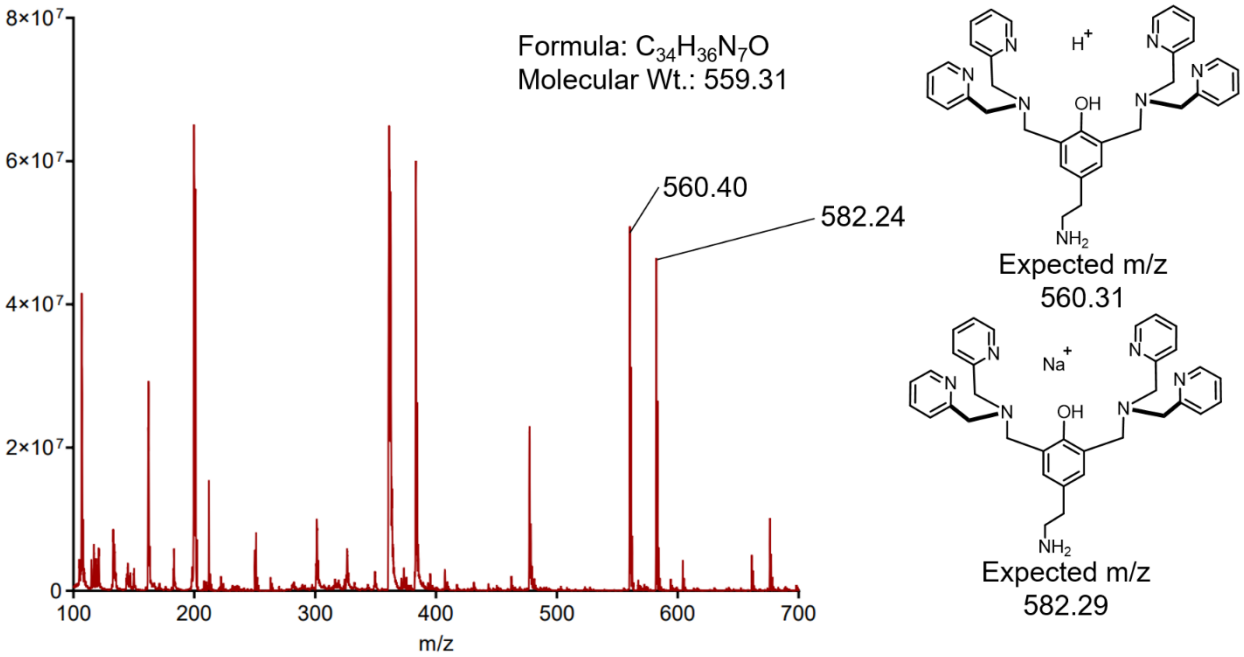

Figure S19: ESI MS of 4-(2-aminoethyl)-2,6-bis((bis(pyridin-2-ylmethyl) amino) methyl)phenol (2).

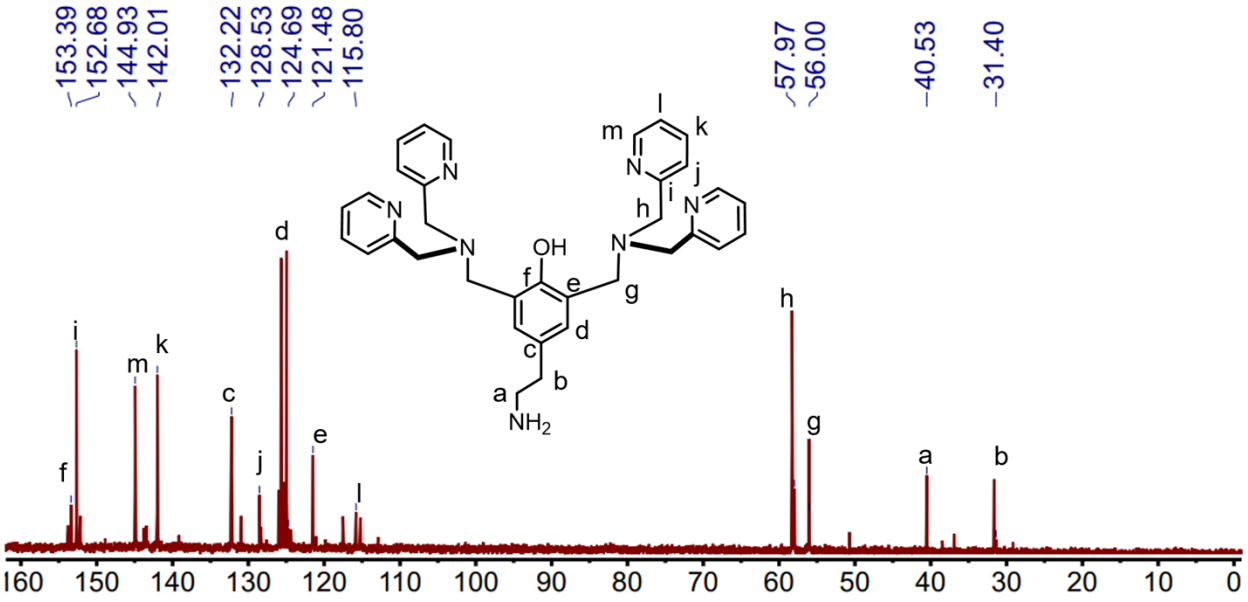

Figure S20: ^{13}C NMR of 4-(2-aminoethyl)-2,6-bis((bis(pyridin-2-ylmethyl) amino) methyl) phenol (2).

Synthesis of Apo version of BactVue:

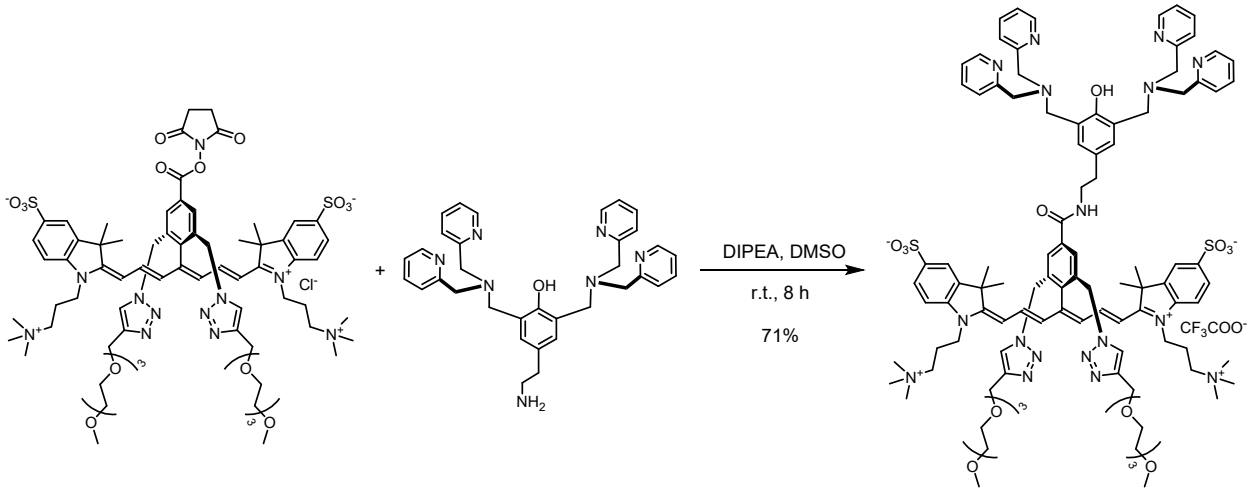

The dye s775z-NHS was prepared during a previous study.[30] A mixture of s775z-NHS (45.00 mg, 29.90 µmol, 1 eq), compound **2** (33.40 mg, 59.70 µmol, 2 eq) and diisopropyl ethyl amine (26.2 µL, 149 µmol, 5 eq) in DMSO (2 mL) was stirred at room temperature in the dark for 8 h. The mixture was directly purified by reverse phase column chromatography (C^{18}, 25 – 35% MeOH in H_2O + 0.1% TFA) to afford the product as a dark green solid. ^{1}H NMR (500 MHz, D2O, 25 ˚C) δ (ppm): 8.51 (d, J = 5.80 Hz, 4H), 8.20 (dd, J = 8.00, 8.00 Hz, 4H), 8.16 (s, 2H), 7.90 (s, 2H), 7.75 – 7.72 (m, 6H), 7.66 (dd, J = 8.00, 6.90 Hz, 4H), 7.57 (s, 2H), 7.27 (d, J = 8.5 Hz, 2H), 6.87 (s, 2H), 6.72 (d, J = 13.2 Hz, 2H), 6.55 (dd, J = 13.4, 13.2 Hz, 2H), 6.24 (d, J = 13.4 Hz, 2H), 5.43 (s, 4H), 4.35 (s, 4H), 4.19 (s, 8H), 4.08 (t, J = 6.0 Hz, 8H), 3.58 (s, 4H), 3.54 (t, J = 7.6 Hz, 2H), 3.49 – 3.28 (m, 28H), 3.19 (s, 6H), 3.06 (s, 18H), 2.68 (t, J = 7.4 Hz, 2H), 2.19 (br s, 4H), 0.88 (s, 12H).

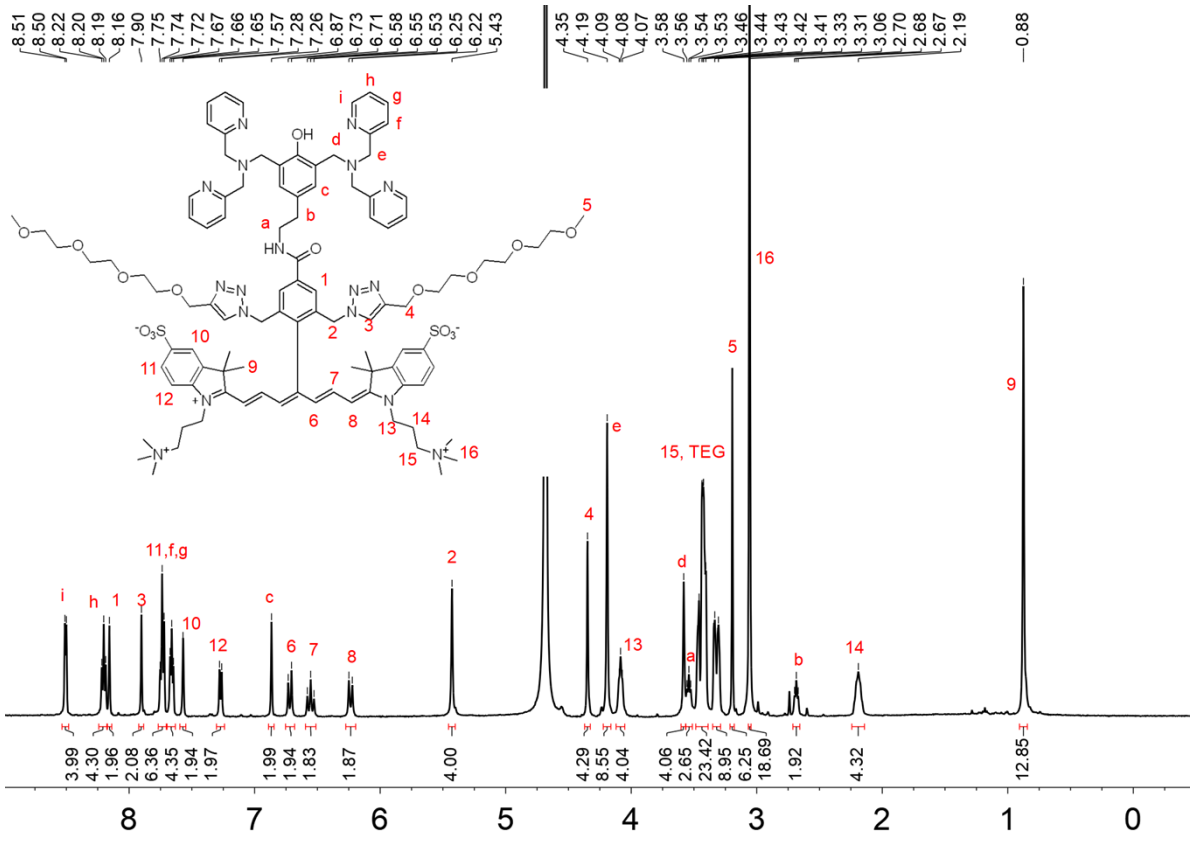

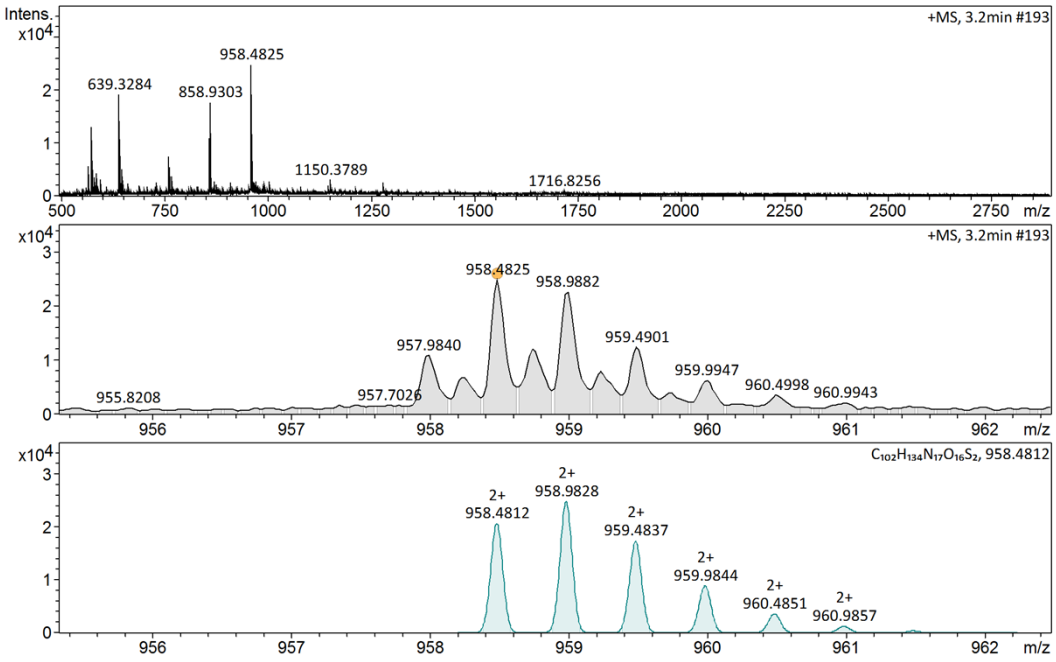

Meas. m/z	#	Ion Formula	m/z	err [ppm]	Mean err [ppm]	rdb	N-Rule	e⁻ Conf	mSigma	Std I	Std Mean m/z	Std I VarNorm	Std m/z Diff	Std Comb Dev
958.482469	1	C102H134N17O16S2	958.481246	-1.3	952.8	44.5	ok	odd	124.9	118.2	n.a.	n.a.	n.a.	n.a.

Figure S21: ^{1}H NMR and ESI-MS of Apo version of BactVue.

Synthesis of BactVue: Apo version of BactVue was treated with two equivalents of $Zn(NO_3)_2$ in methanol and stirred at room temperature for 30 min. The solvent was evaporated to obtain BactVue.

Synthesis of Anionic control dye

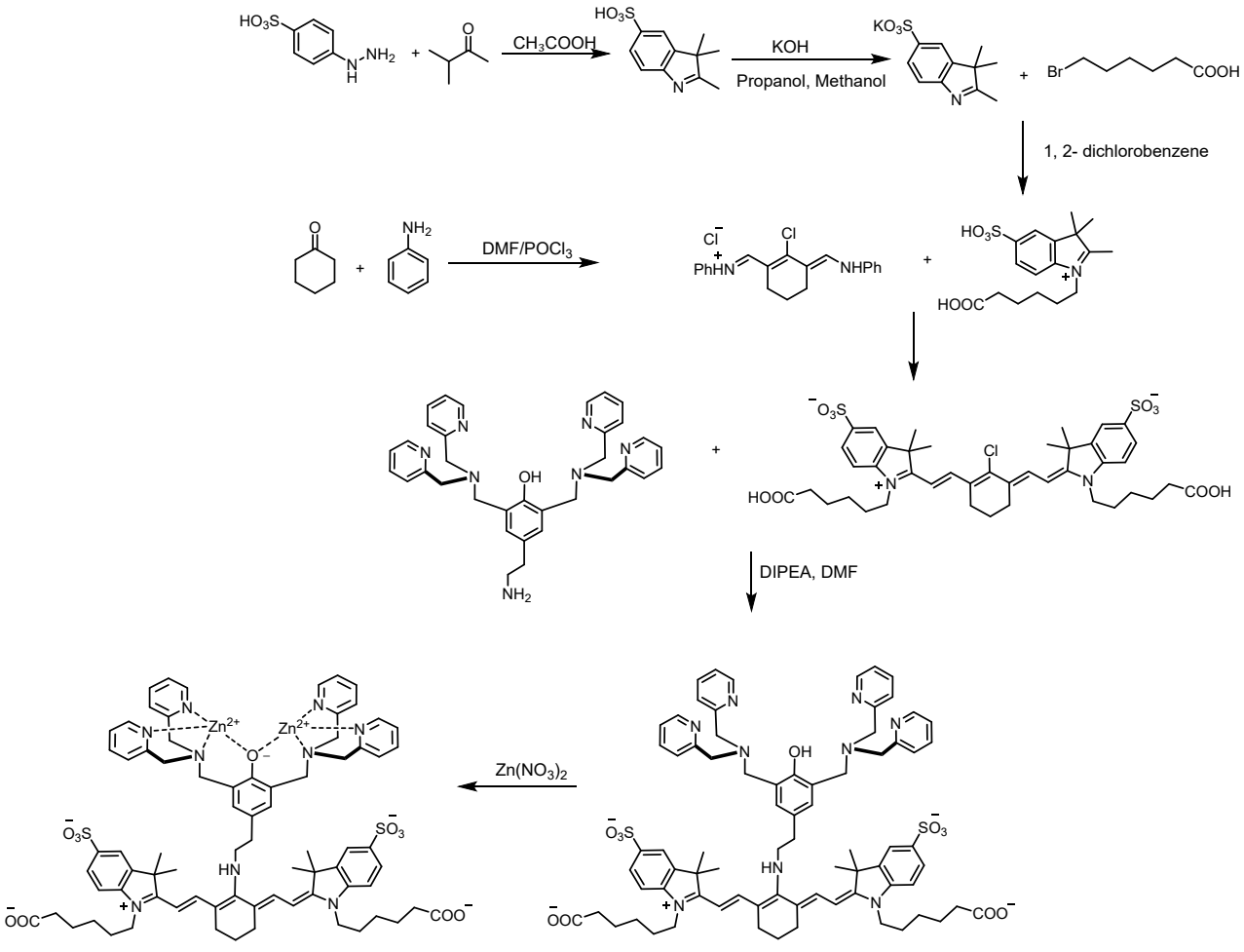

Scheme S6: Synthesis of Anionic control dye.

Synthesis of (3)

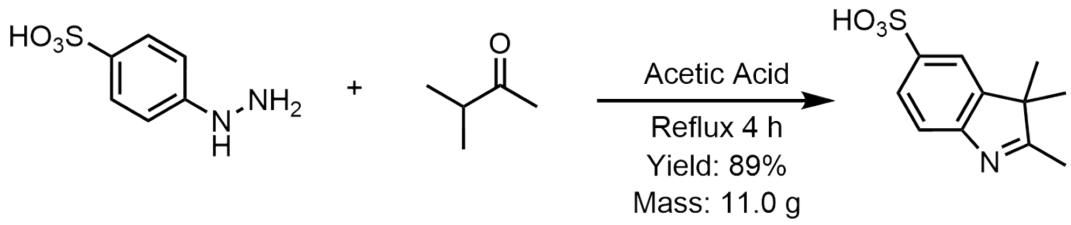

p-Hydrazinobenzenesulfonic acid (10.00 g, 53.00 mmol) and 3-methyl-2-butanone (17 mL, 160 mmol) were dissolved in acetic acid (30.00 mL) and heated at 130˚ C for 4 hours. Then, the reaction flask was cooled to room temperature, and the solid product was filtered. The solid product was washed with ethyl acetate and later dried under reduced pressure. ^{1}H NMR (600 MHz, D_2O) δ 7.90 (s, 1H), 7.82 (d, 1H), 7.60 (d, 1H), 2.04 (s, 3H), 1.40 (s, 6H).

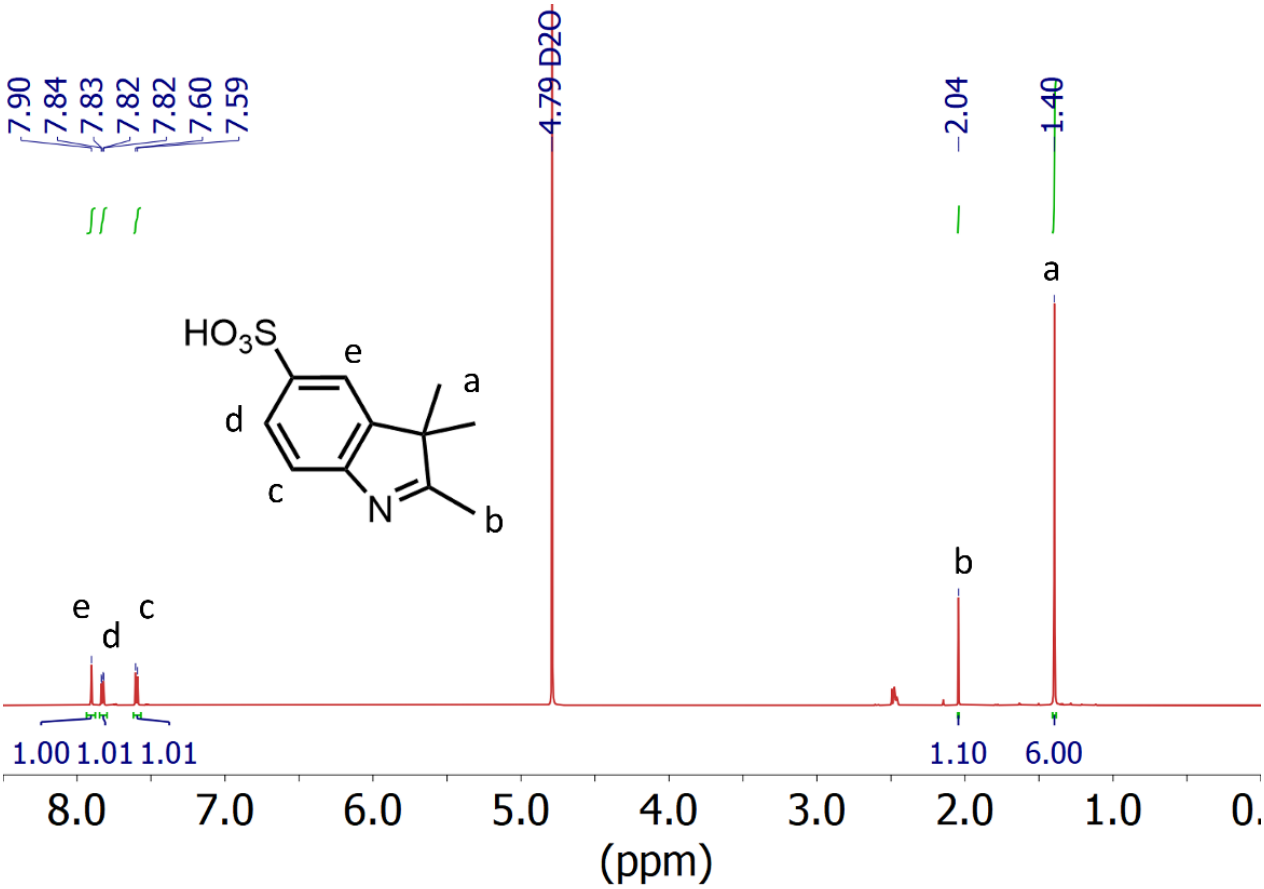

Figure S22:^{1}H NMR of 2,3,3-trimethyl-3H-indole-5-sulfonic acid (3).

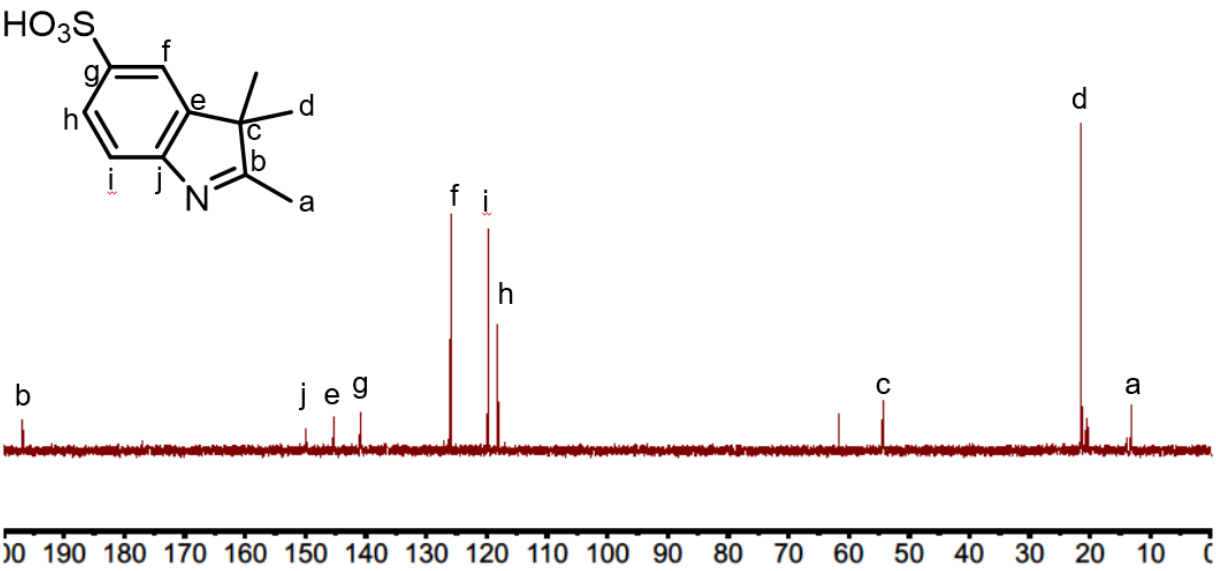

Figure S23: ^{13}C NMR of 2,3,3-trimethyl-3H-indole-5-sulfonic acid (3).

Synthesis of potassium 2,3,3-trimethyl-3H-indole-5-sulfonate (4)

Potassium hydroxide (1.43 g, 25.4 mmol) was dissolved in propanol (35.00 mL). In a separate flask, 2,3,3-trimethyl-3H-indole-5-sulfonic acid (5.07 g, 21.2 mmol) was dissolved in methanol (35.00 mL) and added dropwise to the previous solution and stirred for 24 hours at room temperature. The reaction flask was filtered to obtain 4 as a yellow solids. ^{1}H NMR (600 MHz, D_2O) δ 7.83 (s, 1H), 7.77 (d, 1H), 7.54 (d, 1H), 2.32 (s, 3H), 1.33 (s, 6H).

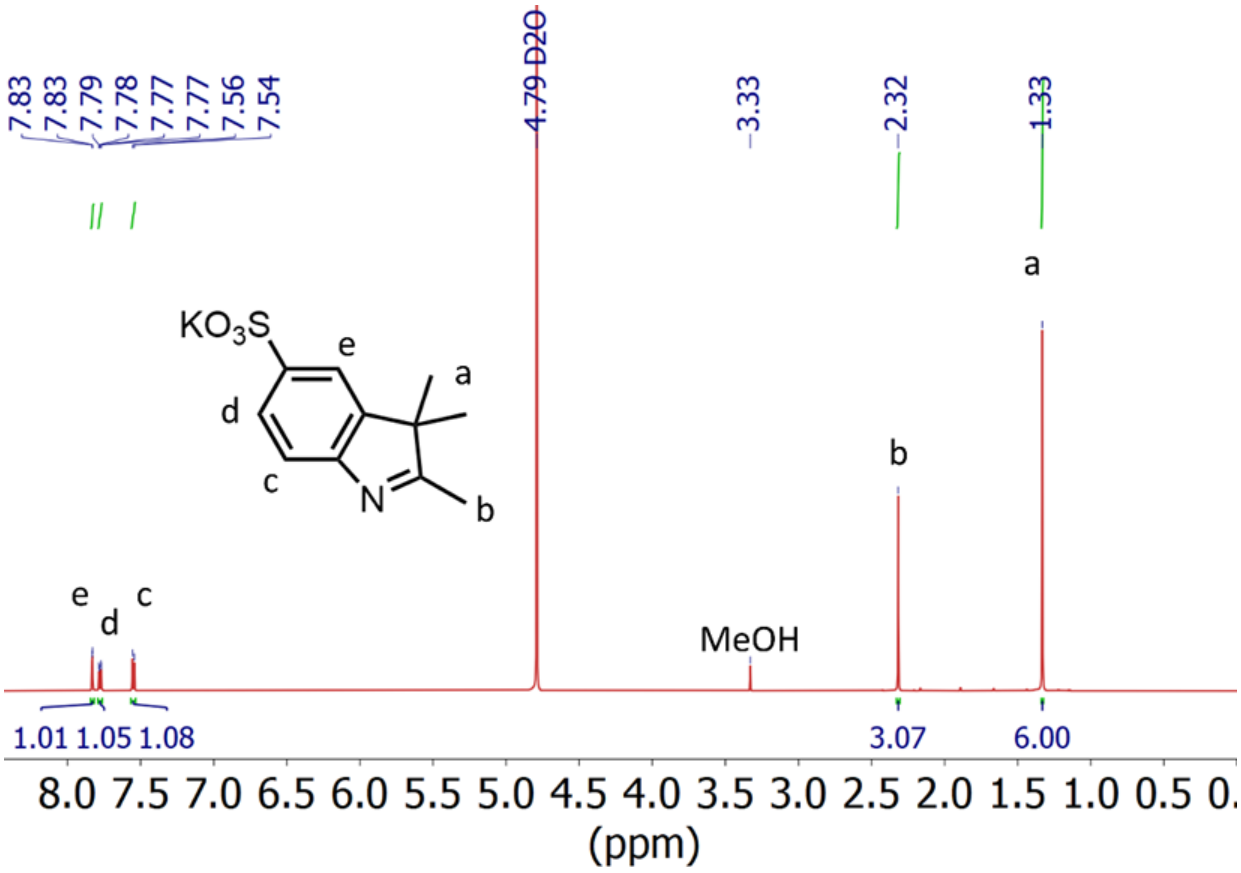

Figure S24: ^{1}H NMR of potassium 2,3,3-trimethyl-3H-indole-5-sulfonate (4).

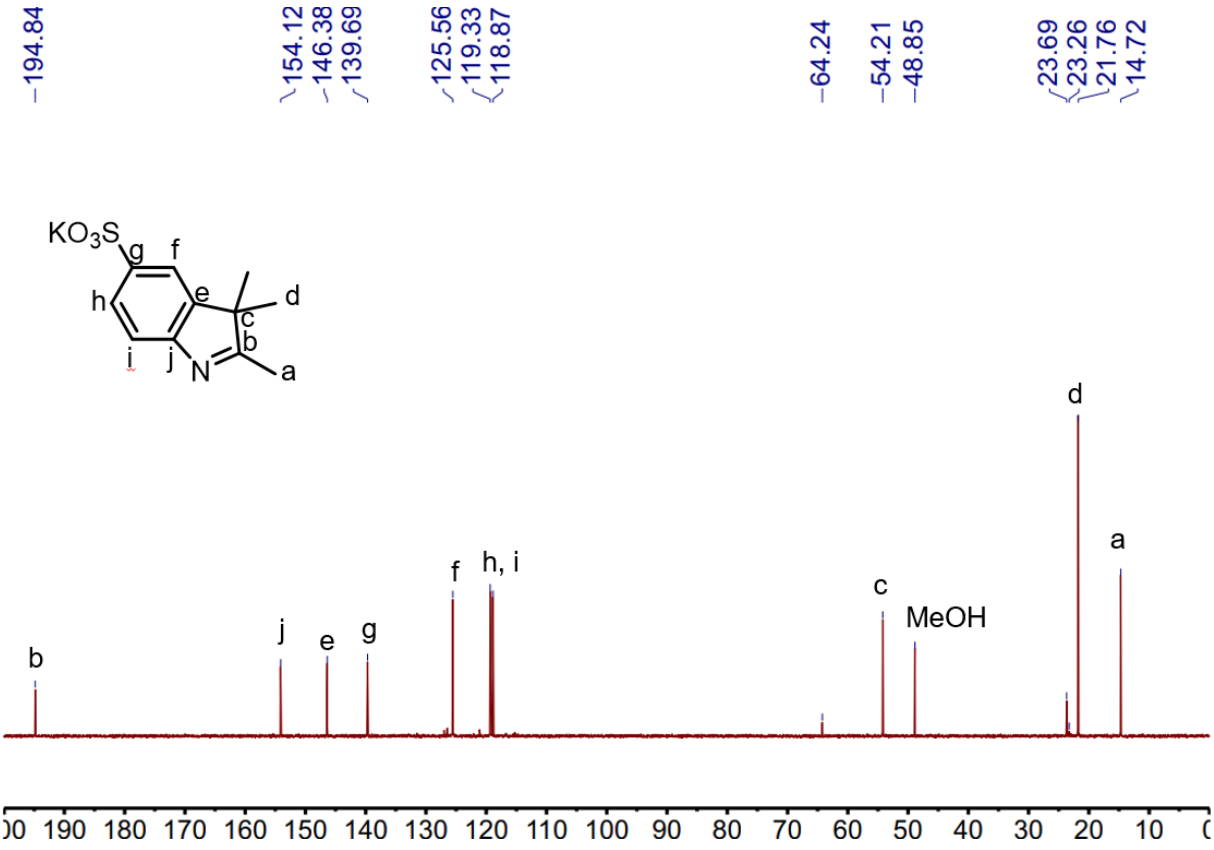

Figure S25:[13]C NMR of potassium 2,3,3-trimethyl-3H-indole-5-sulfonate (4).

Synthesis of 1-(5-carboxypentyl)-2,3,3-trimethyl-5-sulfo-3H-indol-1-ium (5)

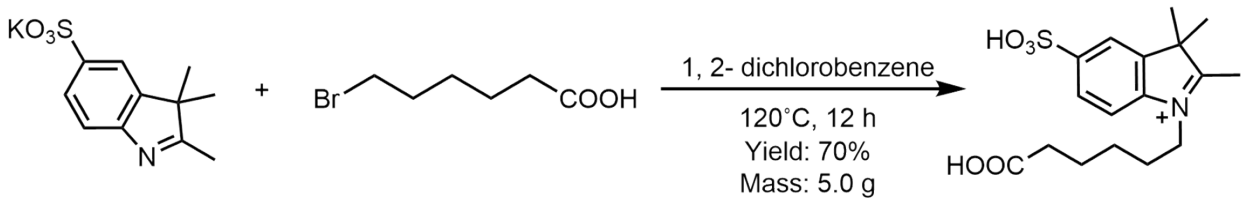

Potassium 2,3,3-trimethyl-3H-indole-5-sulfonate (4) (5 g, 20.9 mmol) and 6-bromohexanoic acid (8.10 g, 41.8 mmol) were dissolved in 1,2-dichlorobenzene (20 mL) and heated at 120 °C for 12 hours. The reaction flask was cooled to room temperature and filtered to collect the solid product. Product 5 was washed with ethyl acetate and later dried under reduced pressure. [1]H NMR (600 MHz, D_2O) δ 8.12 (s, 1H), 8.02 (d, *J* = 8.5 Hz, 1H), 7.89 (d, *J* = 8.6 Hz, 1H), 4.50 (t, *J* = 7.6 Hz,

2H), 2.37 (t, *J* = 7.3 Hz, 2H), 1.65 (p, *J* = 7.2 Hz, 2H), 1.59 (s, 6H), 1.50 (s, 2H), 1.45 (p, *J* = 7.8 Hz, 2H).

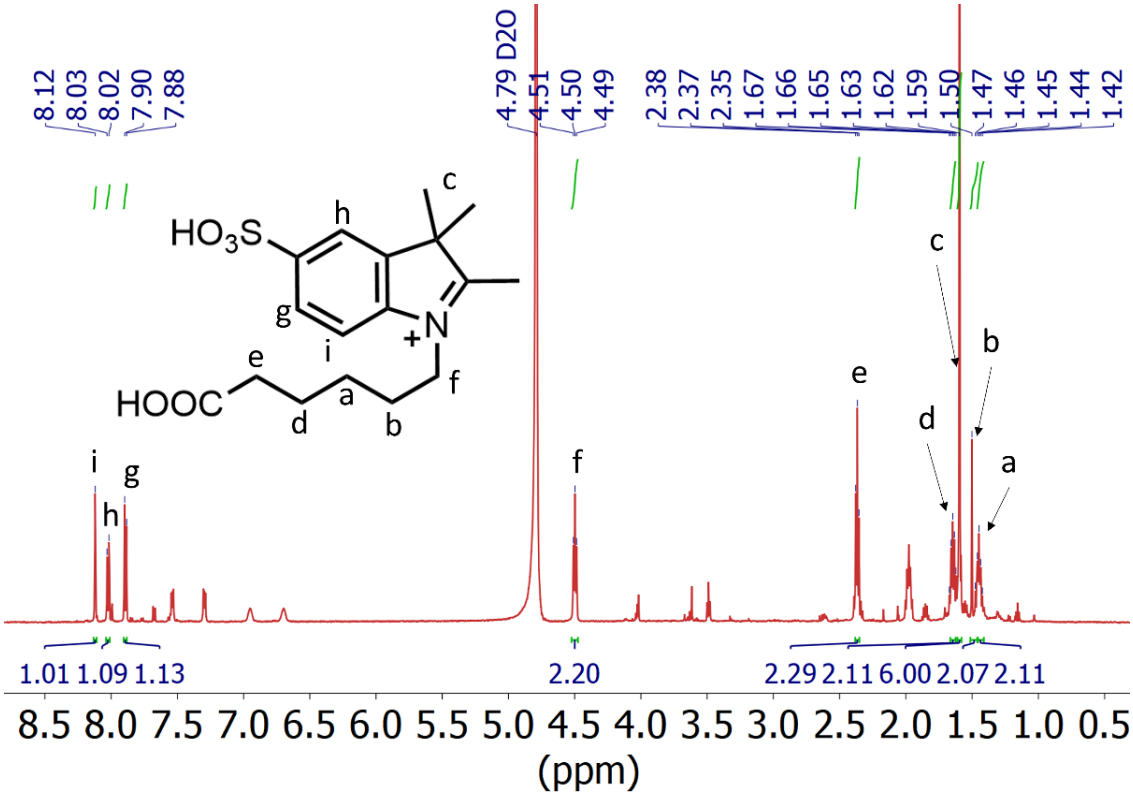

Figure S26: ^{1}H NMR of 1-(5-carboxypentyl)-2,3,3-trimethyl-5-sulfo-3H-indol-1-ium (5).

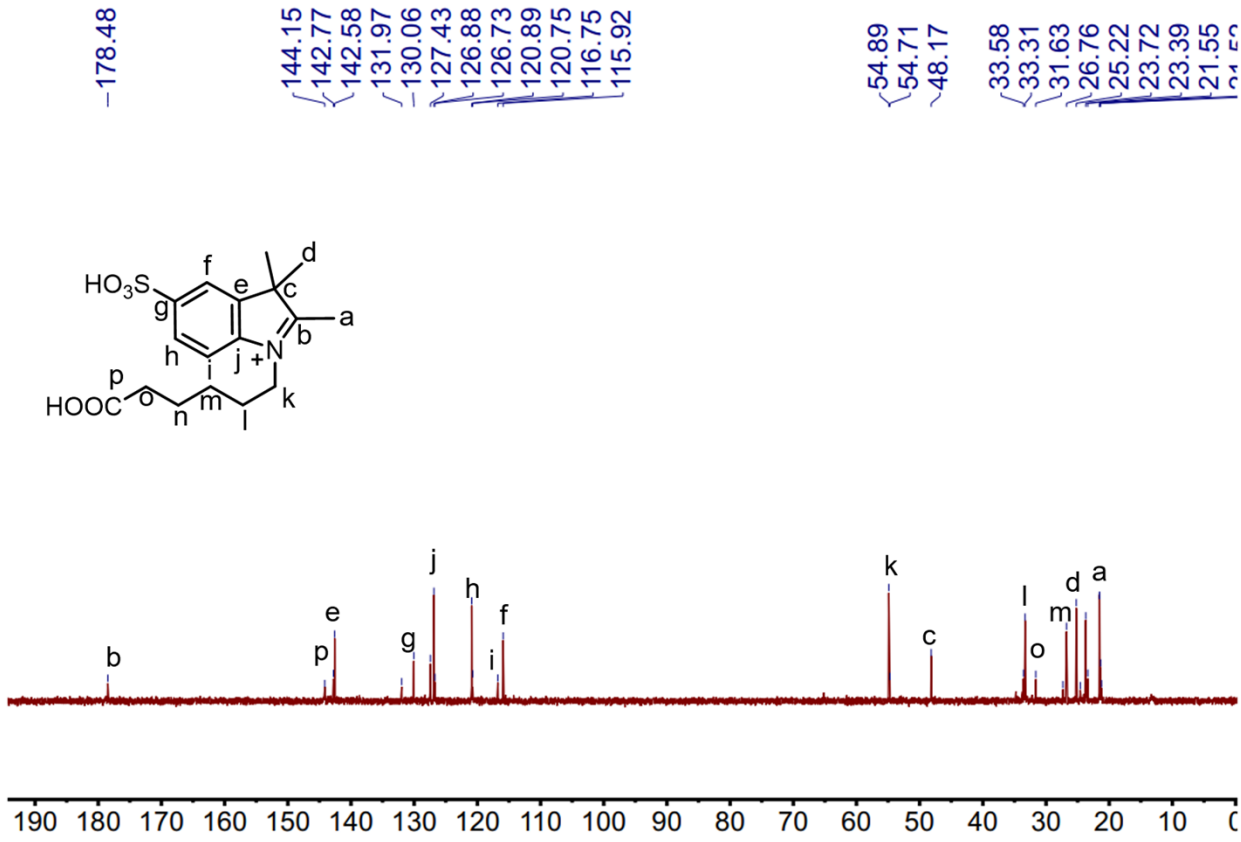

Figure S27: ^{13}C NMR of 1-(5-carboxypentyl)-2,3,3-trimethyl-5-sulfo-3H-indol-1-ium (5).

Synthesis of 2-chloro-3-((phenylamino)methylene)cyclohex-1-en-1 yl)methylene)benzenaminium (6)

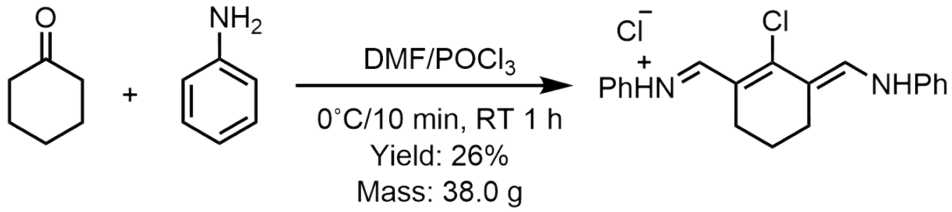

DMF (60 mL) and DCM (40 mL) were mixed and cooled to 0 °C using an ice bath. In a separate flask, phosphorus oxychloride (45.2 ml, 1.50 mol) was dissolved in DCM (40 mL) and added to the previous reaction flask dropwise over 10 minutes. Cyclohexanone (11.7 ml, 0.40 mol) was added dropwise over 10 min to the reaction flask. The reaction flask was removed from the ice bath and heated to reflux for 3 hours. The reaction flask was cooled to room temperature, and

aniline (31 ml, 1 mol) was added and stirred at room temperature for an additional 1 hour. Distilled water (50 mL) was added to the reaction flask and refrigerated overnight. The following day, the solid particles were filtered, collected, and purified by silica chromatography (gradient 0-20 % Methanol in DCM) to yield 6 as a purple solid. ^{1}H NMR (600 MHz, MeOD) δ 8.71 (s, 2H), 7.49 (s, 4H), 7.39 (s, 4H), 7.33 (s, 2H), 6.67 (s, 2H), 2.74 (t, J = 6.2 Hz, 4H), 2.01 (p, J = 6.6 Hz, 2H).

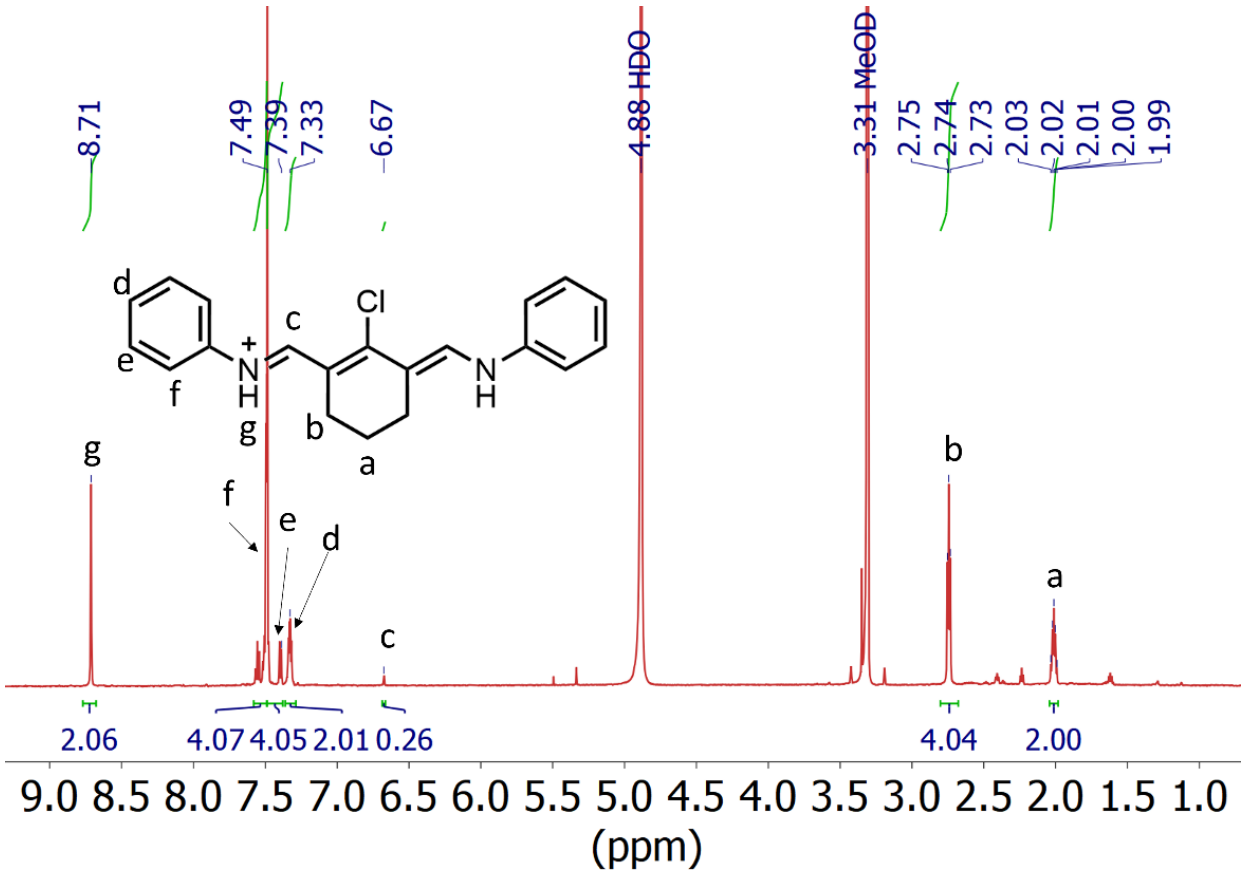

Figure S28: ^{1}H NMR of 2-chloro-3-(phenylamino)methylene)cyclohex-1-en-1-yl)methylene)benzenaminium (6).

Synthesis of (E)-1-(5-carboxypentyl)-2-((E)-2-(3-((E)-2-(1-(5-carboxypentyl)-3,3-dimethyl-5-sulfo-3H-indol-1-ium-2-yl)vinyl)-2-chlorocyclohex-2-en-1-ylidene)ethylidene)-3,3-dimethylindoline-5-sulfonate (7)

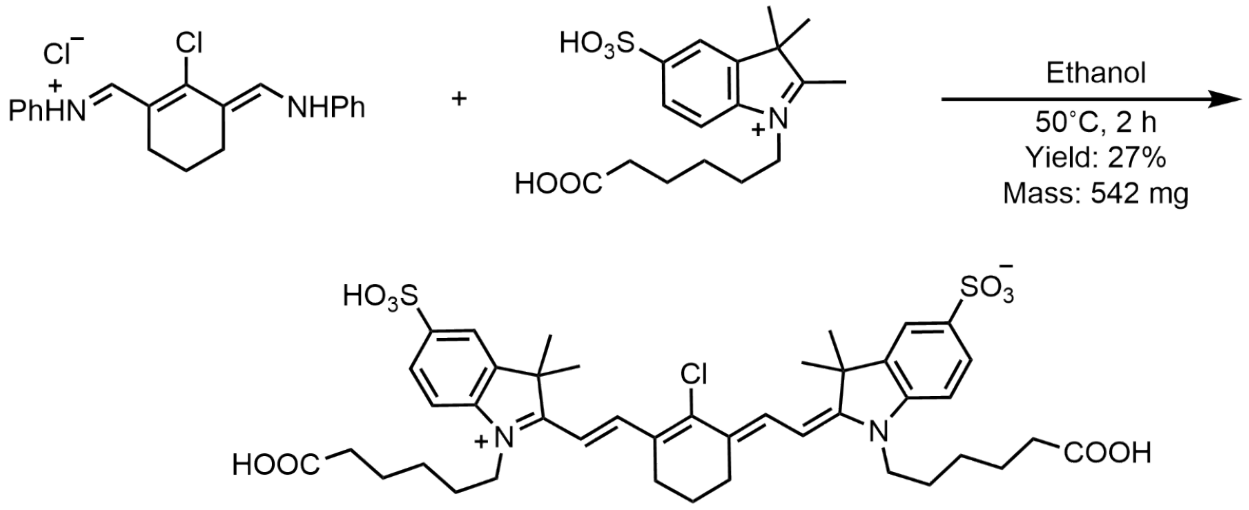

1-(5-carboxypentyl)-2,3,3-trimethyl-5-sulfo-3H-indol-1-ium 5 (1.89 g, 5.34 mmol), 2-chloro-3-((phenylamino)methylene)cyclohex-1-en-1-yl)methylene)benzenaminium 6 (941 mg, 2.67 mmol), and sodium acetate (438 mg, 5.34 mmol) were dissolved in ethanol (20 mL) and heated at 50 °C for 2 hours. After cooling to room temperature, the reaction flask was filtered to collect the solid product. The solid product was washed with ethyl acetate and later dried under reduced pressure. The product was further purified by silica chromatography (gradient 0-40% Methanol in DCM) to yield pure 7 as a green solid. ^{1}H NMR (600 MHz, MeOD) δ 8.47 (d, J = 14.1 Hz, 2H), 7.93 (s, 2H), 7.90 (d, J = 8.3 Hz, 2H), 7.38 (d, J = 8.3 Hz, 2H), 6.34 (d, J = 14.2 Hz, 2H), 2.75 (d, 4H), 2.31 (s, 4H), 1.87 (q, 4H), 1.76 (d, 12H), 1.70 (s, 4H), 1.61 (q, 2H), 1.51 (d, 4H), 1.29 (q, 4H).

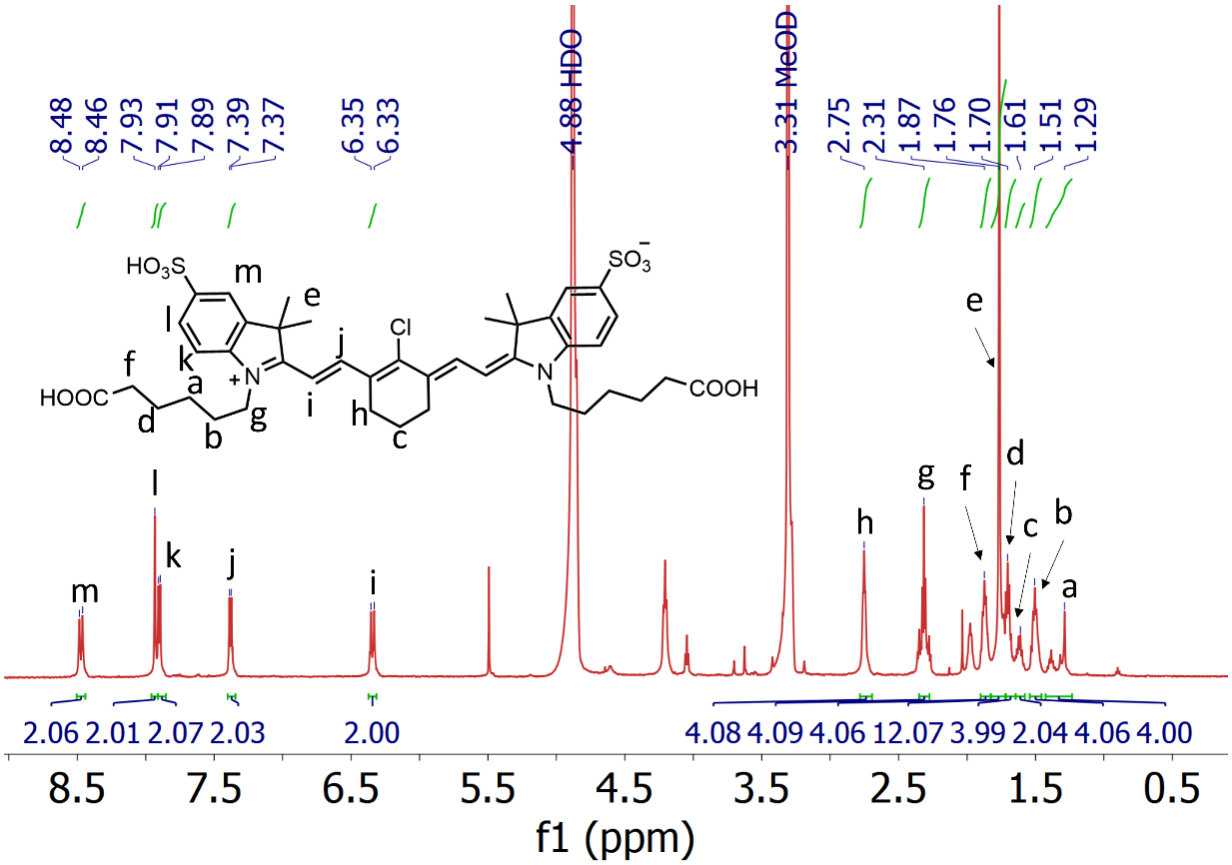

Figure S29: ^{1}H NMR of (E)-1-(5-carboxypentyl)-2-((E)-2-(3-((E)-2-(1-(5-carboxypentyl)-3,3-dimethyl-5-sulfo-3H-indol-1-ium-2-yl)vinyl)-2-chlorocyclohex-2-en-1-ylidene)ethylidene)-3,3-dimethylindoline-5-sulfonate (7).

Synthesis of 2-((E)-2-((E)-2-((3-((bis(pyridin-2-ylmethyl)amino)methyl)-4-hydroxy-5-(((pyridin-2-ylmethyl)(pyridin-3-ylmethyl)amino)methyl)phenethyl)amino)-3-(2-((E)-1-(5-carboxypentyl)-3,3-dimethyl-5-sulfonatoindolin-2-ylidene)ethylidene)cyclohex-1-en-1-yl)vinyl)-1-(5-carboxypentyl)-3,3-dimethyl-3H-indol-1-ium-5-sulfonate (Apo version of Anionic control dye).

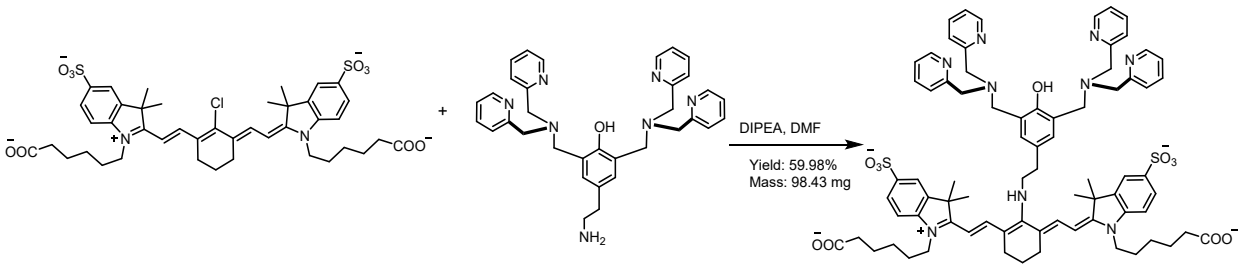

A mixture of compound **7** (100.00 mg, 118.62 µmol, 1 eq), compound **2** (329.0 mg, 58.85 µmol, 5 eq), and diisopropyl ethyl amine (76 µL, 59 µmol, 5 eq) in DMF (5 mL) was stirred at 50°C for 12 hours. The mixture was further purified by silica chromatography (gradient 0-60 % Methanol in DCM) to yield a green solid (98.43 mg, 59.98 %). ^{1}H NMR (600 MHz, MeOD) δ 8.57 (s, 4H), 8.45 (d, *J* = 14.2 Hz, 2H), 7.96 (s, 2H), 7.91 (d, *J* = 11.4 Hz, 2H), 7.88 – 7.83 (m, 2H), 7.79 (s, 4H), 7.43 (d, *J* = 7.9 Hz, 4H), 7.38 (s, 4H), 7.13 (s, 2H), 6.33 (d, *J* = 14.0 Hz, 2H), 4.27 (s, 8H), 4.16 (s, 4H), 3.21 (d, *J* = 7.4 Hz, 4H), 2.98 (s, 4H), 2.85 (s, 4H), 2.74 (t, *J* = 5.9 Hz, 2H), 2.68 (s, 4H), 2.14 (s, 4H), 1.86 (d, *J* = 14.9 Hz, 2H), 1.74 (s, 4H), 1.68 (t, *J* = 7.6 Hz, 2H), 1.36 (s, 12H).

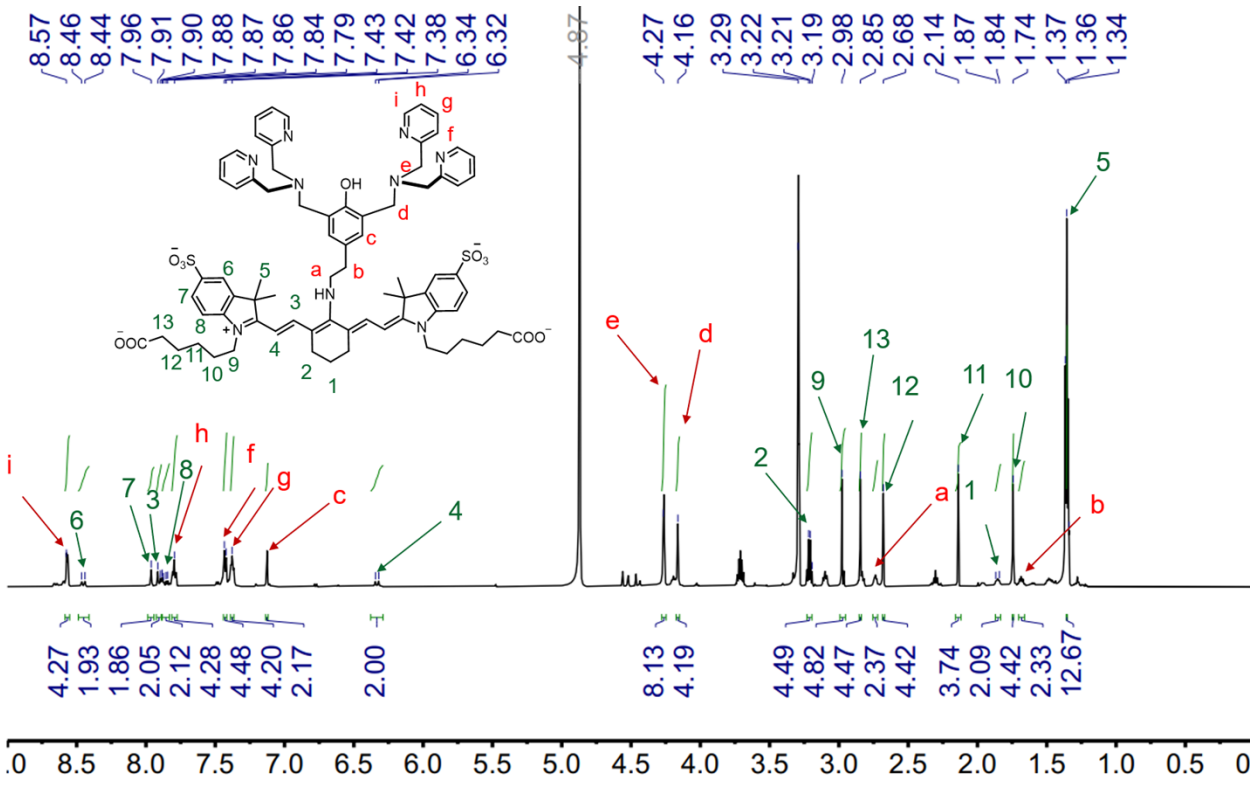

Figure S30: ^{1}H NMR apo version of Anionic control dye.

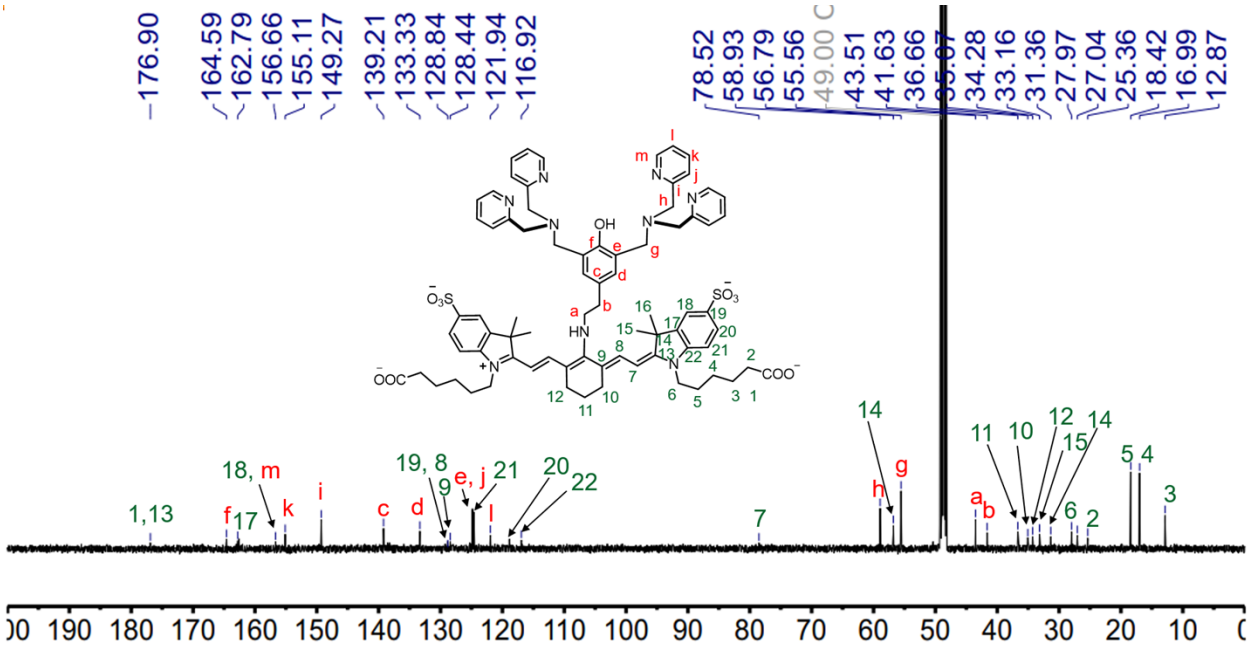

Figure S31: C^{13} NMR of the apo version of Anionic control dye.

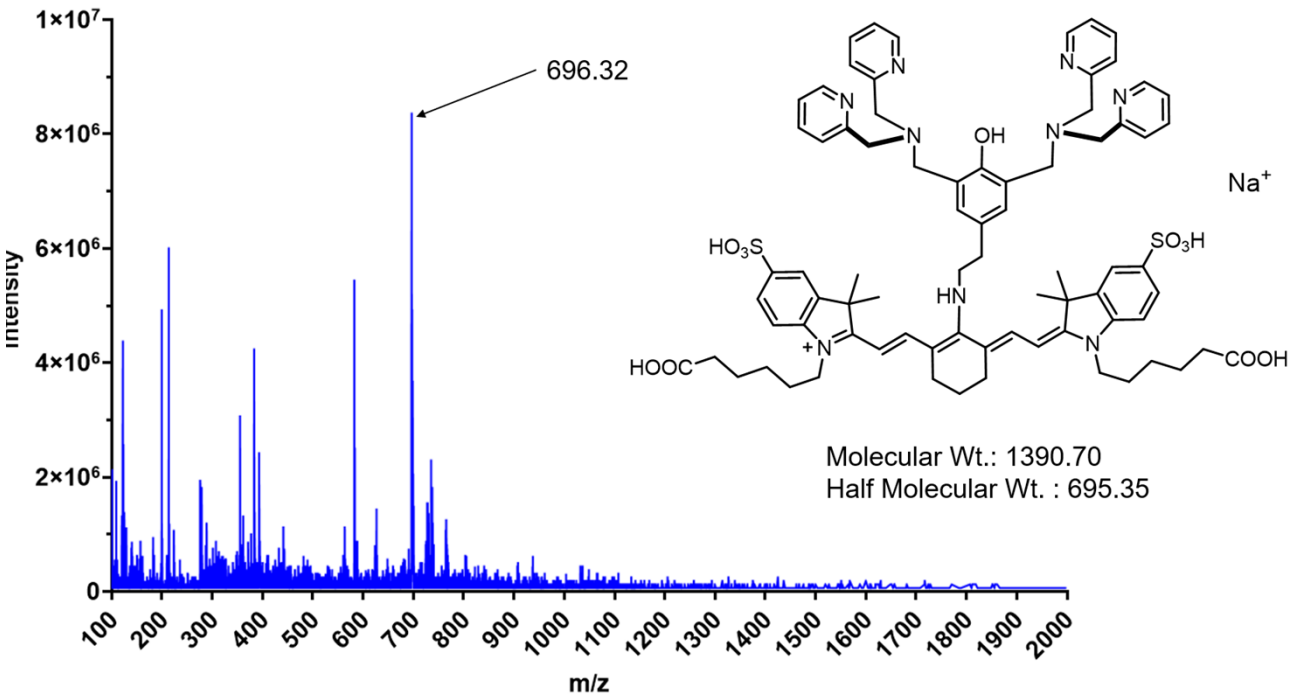

Figure S32: ESI-MS of the apo version of Anionic control dye.

Synthesis of Anionic control dye: The apo version was treated with two equivalents of Zn $(NO_3)_2$ in methanol and stirred at room temperature for 30 min. The solvent was evaporated to obtain Anionic control dye.

References

1. D. R. Rice, K. J. Clear and B. D. Smith, Imaging and therapeutic applications of zinc (ii)-dipicolylamine molecular probes for anionic biomembranes, *Chemical Communications*, 2016, **52**, 8787-8801.
2. C. Lakshmi, R. G. Hanshaw and B. D. Smith, Fluorophore-linked zinc (II) dipicolylamine coordination complexes as sensors for phosphatidylserine-containing membranes, *Tetrahedron*, 2004, **60**, 11307-11315.
3. K. J. Clear, K. M. Harmatys, D. R. Rice, W. R. Wolter, M. A. Suckow, Y. Wang, M. Rusckowski and B. D. Smith, Phenoxide-bridged zinc (II)-bis (dipicolylamine) probes for molecular imaging of cell death, *Bioconjugate chemistry*, 2016, **27**, 363-375.
4. H. Jiang, E. J. O'neil, K. M. DiVittorio and B. D. Smith, Anion-mediated phase transfer of zinc (II)-coordinated tyrosine derivatives, *Organic letters*, 2005, **7**, 3013-3016.
5. K. M. DiVittorio, W. M. Leevy, E. J. O'Neil, J. R. Johnson, S. Vakulenko, J. D. Morris, K. D. Rosek, N. Serazin, S. Hilkert and S. Hurley, Zinc (II) coordination complexes as membrane-active fluorescent probes and antibiotics, *ChemBioChem*, 2008, **9**, 286-293.
6. F. M. Roland, E. M. Peck, D. R. Rice and B. D. Smith, Preassembled fluorescent multivalent probes for the imaging of anionic membranes, *Bioconjugate chemistry*, 2017, **28**, 1093-1101.
7. H. Jiang, J. O'Neil E, K. M. Divittorio and B. D. Smith, Anion-mediated phase transfer of Zinc(II)-coordinated tyrosine derivatives, *Org Lett*, 2005, **7**, 3013-3016.
8. J. R. Johnson, H. Jiang and B. D. Smith, Zinc (II)-coordinated oligotyrosine: a new class of cell penetrating peptide, *Bioconjugate chemistry*, 2008, **19**, 1033-1039.
9. K. J. Clear, K. M. Harmatys, D. R. Rice, W. R. Wolter, M. A. Suckow, Y. Wang, M. Rusckowski and B. D. Smith, Phenoxide-Bridged Zinc(II)-Bis(dipicolylamine) Probes for Molecular Imaging of Cell Death, *Bioconjug Chem*, 2016, **27**, 363-375.
10. K. M. Harmatys, A. J. Musso, K. J. Clear and B. D. Smith, Small molecule additive enhances cell uptake of 5-aminolevulinic acid and conversion to protoporphyrin IX, *Photochemical & Photobiological Sciences*, 2016, **15**, 1408-1416.
11. E. J. O'Neil, H. Jiang and B. D. Smith, Effect of bridging anions on the structure and stability of phenoxide bridged zinc dipicolylamine coordination complexes, *Supramolecular chemistry*, 2013, **25**, 315-322.
12. H. T. Ngo, X. Liu and K. A. Jolliffe, Anion recognition and sensing with Zn(II)-dipicolylamine complexes, *Chem Soc Rev*, 2012, **41**, 4928-4965.
13. D. R. Rice, H. Gan and B. D. Smith, Bacterial imaging and photodynamic inactivation using zinc (II)-dipicolylamine BODIPY conjugates, *Photochemical & Photobiological Sciences*, 2015, **14**, 1271-1281.
14. W. M. Leevy, S. T. Gammon, H. Jiang, J. R. Johnson, D. J. Maxwell, E. N. Jackson, M. Marquez, D. Piwnica-Worms and B. D. Smith, Optical imaging of bacterial infection in living mice using a fluorescent near-infrared molecular probe, *Journal of the American Chemical Society*, 2006, **128**, 16476-16477.
15. W. MatthewáLeevy, Selective recognition of bacterial membranes by zinc (II)-coordination complexes, *Chemical communications*, 2006, 1595-1597.
16. A. G. White, N. Fu, W. M. Leevy, J.-J. Lee, M. A. Blasco and B. D. Smith, Optical imaging of bacterial infection in living mice using deep-red fluorescent squaraine rotaxane probes, *Bioconjugate chemistry*, 2010, **21**, 1297-1304.
17. W. M. Leevy, S. T. Gammon, J. R. Johnson, A. J. Lampkins, H. Jiang, M. Marquez, D. Piwnica-Worms, M. A. Suckow and B. D. Smith, Noninvasive optical imaging of staphylococcus aureus bacterial infection in living mice using a Bis-dipicolylamine-Zinc (II) affinity group conjugated to a near-infrared fluorophore, *Bioconjugate chemistry*, 2008, **19**, 686-692.

18. B. M. Sharon, A. P. Arute, A. Nguyen, S. Tiwari, S. S. Reddy Bonthu, N. V. Hulyalkar, M. L. Neugent, D. Palacios Araya, N. A. Dillon and P. E. Zimmern, Genetic and functional enrichments associated with Enterococcus faecalis isolated from the urinary tract, *Mbio*, 2023, **14**, e02515-02523.
19. I. D. Pogozheva, G. A. Armstrong, L. Kong, T. J. Hartnagel, C. A. Carpino, S. E. Gee, D. M. Picarello, A. S. Rubin, J. Lee and S. Park, Comparative molecular dynamics simulation studies of realistic eukaryotic, prokaryotic, and archaeal membranes, *Journal of chemical information and modeling*, 2022, **62**, 1036-1051.
20. S. Feng, S. Park, Y. K. Choi and W. Im, CHARMM-GUI membrane builder: past, current, and future developments and applications, *Journal of chemical theory and computation*, 2023, **19**, 2161-2185.
21. M. J. Frisch, G. W. Trucks, H. B. Schlegel, G. E. Scuseria, M. A. Robb, J. R. Cheeseman, G. Scalmani, V. Barone, G. A. Petersson, H. Nakatsuji, X. Li, M. Caricato, A. V. Marenich, J. Bloino, B. G. Janesko, R. Gomperts, B. Mennucci, H. P. Hratchian, J. V. Ortiz, A. F. Izmaylov, J. L. Sonnenberg, Williams, F. Ding, F. Lipparini, F. Egidi, J. Goings, B. Peng, A. Petrone, T. Henderson, D. Ranasinghe, V. G. Zakrzewski, J. Gao, N. Rega, G. Zheng, W. Liang, M. Hada, M. Ehara, K. Toyota, R. Fukuda, J. Hasegawa, M. Ishida, T. Nakajima, Y. Honda, O. Kitao, H. Nakai, T. Vreven, K. Throssell, J. A. Montgomery Jr., J. E. Peralta, F. Ogliaro, M. J. Bearpark, J. J. Heyd, E. N. Brothers, K. N. Kudin, V. N. Staroverov, T. A. Keith, R. Kobayashi, J. Normand, K. Raghavachari, A. P. Rendell, J. C. Burant, S. S. Iyengar, J. Tomasi, M. Cossi, J. M. Millam, M. Klene, C. Adamo, R. Cammi, J. W. Ochterski, R. L. Martin, K. Morokuma, O. Farkas, J. B. Foresman and D. J. Fox, Gaussian 16 Rev. C.01.*Journal*, 2016.
22. D. A. Case, H. M. Aktulga, K. Belfon, D. S. Cerutti, G. A. Cisneros, V. W. D. Cruzeiro, N. Forouzesh, T. J. Giese, A. W. Götz and H. Gohlke, AmberTools, *Journal of chemical information and modeling*, 2023, **63**, 6183-6191.
23. D. J. Price and C. L. Brooks III, A modified TIP3P water potential for simulation with Ewald summation, *The Journal of chemical physics*, 2004, **121**, 10096-10103.
24. R. Salomon-Ferrer, A. W. Gotz, D. Poole, S. Le Grand and R. C. Walker, Routine microsecond molecular dynamics simulations with AMBER on GPUs. 2. Explicit solvent particle mesh Ewald, *Journal of chemical theory and computation*, 2013, **9**, 3878-3888.
25. A. W. Gotz, M. J. Williamson, D. Xu, D. Poole, S. Le Grand and R. C. Walker, Routine microsecond molecular dynamics simulations with AMBER on GPUs. 1. Generalized born, *Journal of chemical theory and computation*, 2012, **8**, 1542-1555.
26. W. Humphrey, A. Dalke and K. Schulten, VMD: visual molecular dynamics, *Journal of molecular graphics*, 1996, **14**, 33-38.
27. L. Schrödinger and W. DeLano, The PyMOL Molecular Graphics System, V2. 0.0, *Schrödinger, LLC, New York, NY*, 2019.
28. J. D. Hunter, Matplotlib: A 2D graphics environment, *Computing in science & engineering*, 2007, **9**, 90-95.
29. C.-S. Hung, K. W. Dodson and S. J. Hultgren, A murine model of urinary tract infection, *Nature protocols*, 2009, **4**, 1230-1243.
30. D. H. Li, C. L. Schreiber and B. D. Smith, Sterically Shielded Heptamethine Cyanine Dyes for Bioconjugation and High Performance Near-Infrared Fluorescence Imaging, *Angew Chem Int Ed Engl*, 2020, **59**, 12154-12161.